UQAR
Université du Québec
à Rimouski

Saturation tourbillonaire du gyre de Beaufort

MÉMOIRE PRÉSENTÉ

dans le cadre du programme de maîtrise en océanographie

en vue de l'obtention du grade de Magister Scientiae

PAR

©MARIA GHETA

Mars 2026

Composition du jury :

Cédric Chavanne, président du jury, Université du Québec à Rimouski

Louis-Philippe Nadeau, directeur de recherche, Université du Québec à Rimouski

David Straub, examinateur externe, McGill University

Dépôt initial le 12 décembre 2025 Dépôt final le 19 mars, 2026

RÉSUMÉ

Le Gyre de Beaufort (BG), situé en Arctique et le Courant Circumpolaire Antarctique (ACC), dans l'océan Austral, présentent plusieurs similarités dynamiques, mais des différences majeures les distinguent également. Dans cette étude, nous évaluons dans quelle mesure les nombreuses connaissances issues de la dynamique du ACC peuvent être transposées au BG. Au-delà de leurs contrastes géométriques, l'Arctique est recouvert de glace de mer, et les interactions glace–océan influencent fortement sa dynamique. De plus, alors que le gradient du paramètre de Coriolis (plan-β) joue un rôle central dans la dynamique de l'ACC, sa variation est faible dans le cas du BG. Le BG est plutôt circonscrit par un bassin topographique qui modifie les contours de vorticité potentielle et peut être interprété comme un effet β topographique. Nos résultats montrent que, bien que la dynamique de l'ACC puisse effectivement éclairer la compréhension du BG, la présence d'un bassin topographique modifie considérablement sa réponse à la glace de mer et à la circulation de renversement. Une distinction claire apparaît entre le rôle de la topographie azimutale (alignée avec le vent), représentant le talus continental, et celui de la topographie radiale (perpendiculaire au vent), représentant une dorsale sous-marine. La topographie azimutale joue un rôle similaire à celui du plan-β : elle stabilise l'écoulement en modifiant la turbulence locale, renforçant ainsi le transport du BG. À l'inverse, la topographie radiale agit comme une dorsale bloquante en profondeur, permettant la saturation complète du transport. La glace de mer et la circulation de renversement exercent peu d'influence sur le transport en absence de topographie azimutale, mais leur rôle devient important lorsqu'elle est présente. On considère également que l'alignement entre la topographie azimutale et le forçage de surface influence le transport, constituant un mécanisme expliquant la réponse à la couverture de glace et à la circulation de renversement.

Mots clés : Océan Arctique, Gyre de Beaufort, circulation à grande échelle, effets topographiques, glace de mer, circulation de renversement, Courant Circumpolaire Antarctique

ABSTRACT

We assess the extent to which insights from the dynamics of the Antarctic Circumpolar Current (ACC) can be applied to the Beaufort Gyre (BG). Although the two systems share clear similarities, several key differences must be considered. Beyond geometric contrasts, the Arctic is covered by sea ice, and ice–ocean interactions strongly influence its dynamics. Moreover, while the Coriolis parameter gradient (β-plane) plays a central role in ACC dynamics, its variation is weak in the Arctic. Instead, the BG is bounded by a topographic bowl that reshapes geostrophic contours and can be reinterpreted as an effective β-plane. Our results show that, although ACC dynamics can indeed inform our understanding of the BG, the topographic bowl substantially modifies its sensitivity to sea ice and overturning circulation. A distinction emerges between the role of azimuthal topography (aligned with the wind) and radial topography (perpendicular to the wind). Azimuthal topography acts analogously to the β-plane : it modifies turbulence locally in a way that stabilizes the flow and tends to enhance BG transport. In contrast, radial topography acts like a blocking ridge at depth, enabling full transport saturation. Sea ice and overturning circulation exert little influence on transport in the absence of azimuthal topography, but their role becomes significant when it is present. We show that the alignment between the azimuthal topography and the surface forcing influences the transport, constituting a mechanism that explains the effect of ice cover and overturning circulation.

Keywords : Arctic Ocean, Beaufort Gyre, large-scale circulation, topographic effects, sea ice, overturning circulation, Antarctic Circumpolar Current

TABLE DES MATIÈRES

LISTE DES TABLEAUX

LISTE DES FIGURES

LISTE DES ABRÉVIATIONS

ACC Antarctique circumpolar current

BG Beaufort Gyre

PV Potential vorticity

QG Quasigeostrophy

TFS Topographic form stress

IFS Interfacial form stress

KE Kinetic energy

EKE Eddy kinetic energy

LISTE DES SYMBOLES

L_d	Rayon de déformation de Rossby.
T	Transport
f_0	Paramètre de Coriolis
β	Variation latitudinale du paramètre de Coriolis
β_T	β topographique
g	Gravité
(H_1, H_2)	Épaisseurs de la première et deuxième couche
g'	Gravité réduite
ψ	Fonction de courant
τ	Contrainte de surface
τ^a	Contrainte de l'atmosphère
τ^o	Contrainte de l'océan
τ^i	Contrainte de la glace
ζ	Vorticité relative
$\mathscr{r}$	Friction de fond linéaire
$\mathscr{H}$	Circulation de renversement
h_b	Topographie
A_h	Coefficient hypervisqueux
ρ_o	Densité de l'océan
ρ_a	Densité de l'atmosphère
ρ_i	Densité de la glace
C_{da}	Coefficient de fricton de l'atmosphère
C_{di}	Coefficient de fricton de la glace
ω_i	Vitesse angulaire

h_i Épaisseur de la glace

T_{tw} Transport de vent thermique

h Anomalie d'épaisseur de l'halocline

$\mathbf{u}_a$ Vélocité de l'atmosphère

$\mathbf{u}_o$ Vélocité de l'océan

$\mathbf{u}_i$ Vélocité de la glace

α Concentration de glace

INTRODUCTION GÉNÉRALE

Depuis 1979, le réchauffement de l'Arctique a été près de quatre fois plus rapide que la moyenne mondiale (Rantanen et al., 2022). Ce phénomène, appelé amplification arctique, est l'une des conséquences les plus dramatiques du réchauffement climatique, avec des répercussions significatives sur le climat mondial (Previdi et al., 2021). Un des mécanismes principaux de l'amplification arctique est la perte de glace de mer, via la boucle de rétroaction positive entre l'atmosphère et l'albédo de la glace (Serreze & Barry, 2011). L'océan arctique renferme également une quantité de chaleur suffisante en profondeur pour faire fondre toute la glace de mer (Beer et al., 2023). Cependant, sa stratification par la salinité limite le transfert de cette chaleur vers la surface. Le déclenchement de processus convectifs par la formation de glace favorise la remontée d'eau chaude depuis les profondeurs (Polyakov et al., 2020), amplifiant ainsi la fonte et le réchauffement local. Dans ce contexte, la circulation océanique de l'Arctique joue un rôle clé dans son taux de réchauffement.

0.1 Le gyre de Beaufort

Le gyre de Beaufort domine la circulation à grande échelle du bassin Canadien de l'océan Arctique (fig. 1). Ce gyre est forcé par l'anticyclone atmosphérique de Beaufort, qui entraîne un transport d'Ekman des eaux de surface. Ce transport induit une convergence vers le centre du gyre, accumulant de l'eau froide et douce, issue du ruissellement et de la fonte de glace. Ce mécanisme fait du gyre le réservoir d'eau douce le plus important de l'océan arctique (Proshutinsky et al., 2009). Des variations dans le bilan d'eau douce peuvent avoir des répercussions sur l'état de l'océan Arctique, dont l'étendue de la couverture de glace, le budget énergétique, la structure des masses d'eau, ainsi que sur les processus biologiques (Carmack et al., 2008; Zhang et al., 2020).

La capacité de stockage d'eau douce est directement reliée à l'intensité de la circulation

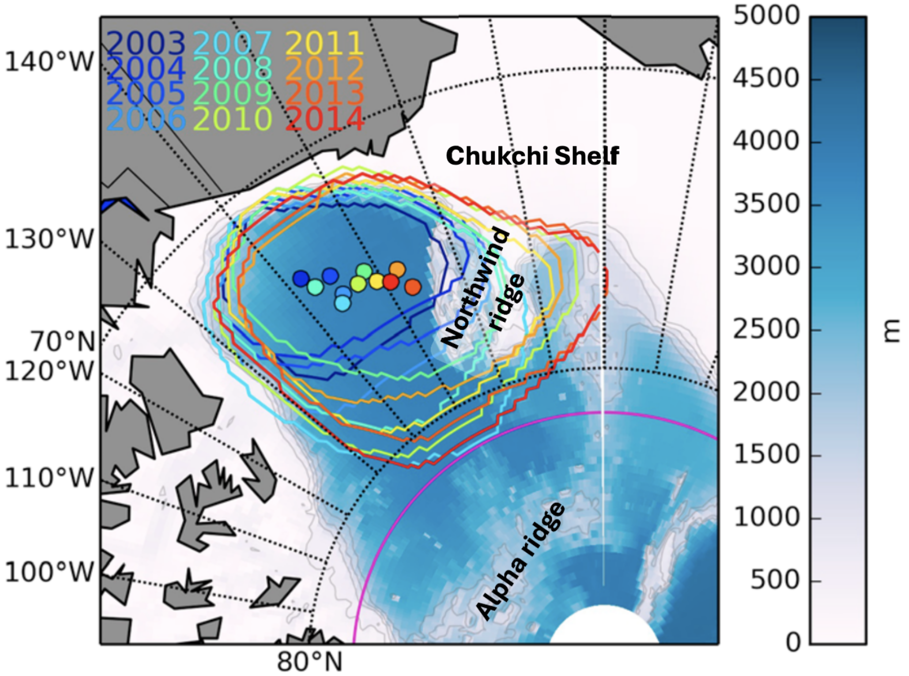

FIGURE 1 – Carte topographique du bassin canadien arctique (champ bleu). L'étendue annuelle du gyre de Beaufort de 2003-2014 est décrite par les courbes colorées, définie par la plus grande courbe fermée de topographie dynamique de la mer. L'emplacement du maximum de la topographie dynamique océanique annuel est indiqué par les points. Figure tirée de Regan et al. (2019), et adaptée pour marquer des caractéristiques topographiques majeures.

du gyre de Beaufort. La convergence d'Ekman à sa surface mène à une plongée des eaux de surface au centre du gyre et à une remontée des eaux profondes sur les bords. Cette circulation verticale accentue la pente des isopycnes du gyre, les déformant en forme de bol, au centre duquel les eaux les plus douces et froides sont "emprisonnées" dans la couche de surface. Plus la pente des isopycnes est accentuée, plus l'intensité du gyre est forte, via la relation du vent thermique :

$$\frac{\partial u}{\partial z} = -\frac{g}{f_0\rho_0}\frac{\partial \rho}{\partial y}, \tag{1}$$

où g est la gravité, ρ_0 est la densité de référence de l'océan, et ρ est la densité. Ceci entraîne une augmentation de la capacité de stockage d'eau douce. Une métrique pour la pente des isopycnes est le transport de vent thermique (T_{tw}). Dans un système à deux couches, ce transport est défini comme :

$$T_{tw} = H_1 \int_0^{Ly} (\langle \overline{\boldsymbol{u}_1} \rangle - \langle \overline{\boldsymbol{u}_2} \rangle) dy. \tag{2}$$

Où H_1 est l'épaisseur de la première couche, Ly est la largeur du domaine, $(\boldsymbol{u}_1, \boldsymbol{u}_2)$ sont la vitesse de la première et la deuxième couche, $\bar{\cdot}$ est une moyenne temporelle et $\langle \cdot \rangle$ est une moyenne méridionale. Plus il y a de cisaillement, plus la pente des isopycnes est grande, menant à un transport de vent thermique plus élevé. Bien que les contraintes de surface soient un mécanisme important régulant le transport de vent thermique du gyre, sous un forçage atmosphérique soutenu, l'intensité du gyre n'augmente pas indéfiniment. Lorsque la pente des isopycnes devient suffisamment abrupte, des instabilités baroclines se développent et génèrent des tourbillons qui tendent à réduire ces pentes. Ce processus a pour conséquence de réduire les pentes isopycnales, ce qui réduit le transport de vent thermique (Manucharyan & Spall, 2016; Doddridge et al., 2019; Timmermans & Toole, 2023). Le courant circumpolaire antarctique (ACC) partage cet équilibre dynamique entre l'accentuation de la pente des isopycnes par les contraintes de surface et l'aplatissement des pentes par les tourbillons. Malgré le fait que les similarités entre l'ACC et le gyre de Beaufort ont été soulignées dans des études idéalisées en Arctique (e.g. Manucharyan & Spall 2016; Yang et al. 2016; Timmermans & Marshall 2020), les liens dynamiques précis qui les relient restent peu clairs. Cette étude propose de s'appuyer sur la littérature abondante de l'ACC afin d'explorer la dynamique du gyre de Beaufort.

0.2 Courant circumpolaire antarctique

La dynamique de l'ACC fait l'objet d'études depuis plus de soixante ans (e.g. Munk & Palmén 1951; Gill 1968). Toutefois, l'intérêt pour la dynamique de la circulation du gyre de Beaufort ne s'est véritablement développé que durant les deux dernières décennies. La richesse de la littérature existante sur l'ACC permet donc d'identifier ses principales caractéristiques dynamiques, sur lesquelles cette étude s'appuie. L'ACC est régi par un équilibre de quantité de mouvement : (i) une injection de quantité de mouvement par le vent, (ii) un transfert par le stress interfacial des couches de surface vers celles en profondeur, et (iii) une dissipation par la topographie. Dans une configuration de canal circumpolaire à fond plat, le frottement est le seul mécanisme dissipant la quantité de mouvement, et le rayon de déformation de Rossby, L_d, régule fortement le transport zonal : $T_{tw} \sim L_d^{1.4}$ (Nadeau & Ferrari, 2015). Le transport dépend aussi du gradient du paramètre de Coriolis, β, et à la contrainte de vent, τ^a, dans le cas à fond plat, mais cette dépendance est relativement plus faible que celle associée à L_d. Par exemple, Gallet & Ferrari (2021) prédisent $T_{tw} \sim L_d^{1.46}\beta^{0.65}\tau^{0.18}$. Une configuration avec une crête sous-marine perpendiculaire à la direction du vent enlève complètement la dépendance du transport aux contraintes du vent. Ce régime est connu sous le nom de saturation tourbillonnaire, et décrit un état dans lequel l'activité des tourbillons contrebalance l'ajout de quantité de mouvement injecté par le vent (Straub, 1993). Dans cette configuration avec une crête, un frottement plus important élimine plus efficacement les tourbillons, ce qui augmente le transport (Nadeau & Ferrari, 2015; Marshall et al., 2017). Indépendamment de la présence ou absence d'une crête dans la topographie, la circulation de renversement module le transport à faible forçage de vent (Youngs et al., 2019). L'ajout de pentes topographiques, représentant la pente continentale de l'Antarctique, introduit un plan-β topographique, créant un jet aligné avec la pente (Thompson, 2010; Stern et al., 2015).

Malgré l'importance reconnue de la topographie, de la friction et de la circulation de renversement dans la dynamique de l'ACC, leur rôle dans le gyre de Beaufort n'est pas bien compris. Dans la section suivante, nous présentons un survol des connaissances actuelles concernant l'influence de ces paramètres physiques sur la circulation du gyre.

0.3 Paramètres physiques

Le gyre de Beaufort comporte une topographie assez complexe, avec le plateau de Chukchi à l'ouest, l'archipel arctique canadien à l'est, la Alpha Ridge au nord, et la Northwind Ridge à l'ouest (fig. 1). Deux types de topographie peuvent être identifiés, (i) la topographie azimutale, due à la pente continentale, et (ii) une topographie plutôt radiale, due aux caractéristiques topographiques qui ne sont pas alignées avec le vent, telle que la Northwind ridge. Comme dans l'ACC, la présence d'une pente topographique azimutale dans le gyre de Beaufort inhibe la formation de tourbillons sur cette pente, intensifiant sa circulation (Manucharyan & Isachsen, 2019), et menant à la formation d'un jet sur la pente (Isachsen et al., 2024; Manucharyan & Isachsen, 2019). La littérature sur l'effet de la topographie radiale dans le gyre de Beaufort est limitée, l'étude de Yang et al. (2016) étant la seule à ce jour à examiner l'effet d'une crête sous-marine dans un gyre de Beaufort idéalisé. Bien que les auteurs aient constaté que la présence d'une crête affaiblit le gyre, leur forçage atmosphérique fixe n'a pas permis d'évaluer si la saturation tourbillonnaire se produit.

La circulation de renversement dans le gyre de Beaufort est due à la circulation double estuarienne de l'Arctique, qui est le résultat d'une plongée des eaux de surface, et une remontée des eaux profondes (Carmack & Wassmann, 2006). La plongée des eaux de surface est due au forçage de flottabilité à la surface, résultant de plusieurs phénomènes, dont la réjection d'eau salée pendant la formation de glace de mer, la turbulence formée à l'interface glace–océan, le mélange par des ondes internes, et le mélange diffusif (Timmermans & Marshall, 2020). Dans leur étude, Lique et al. (2015) démontrent que l'intensité de la circulation des eaux provenant de l'Atlantique a un léger impact sur l'intensité de la circulation du gyre de Beaufort forcé par le vent. Cette étude montre que, à un forçage atmosphérique fixe, l'intensité du gyre n'est influencée par les flux de flottabilité que lorsque la force du mélange est élevée. Cependant, la configuration du modèle numérique utilisé dans cette étude néglige l'effet important des tourbillons. En employant un argument d'analyse d'échelle analytique, Manucharyan & Spall (2016) concluent que l'effet d'une circulation de renversement sur l'intensité du gyre est petit, mais non négligeable lorsque le forçage de vent est faible.

L'effet de la friction sur l'intensité du gyre a été exploré par Nilsson et al. (2024), qui identifient deux régimes limites. Le premier, défini par une faible friction de fond, mène à une réduction du transport de vent thermique du gyre, dû au fait que l'écoulement de la couche du fond est semblable à celui des couches de surface, barotropisant la circulation. Dans la limite d'une forte friction de fond, l'écoulement du fond est réduit, augmentant le cisaillement entre les couches, et donc le transport de vent thermique. Cette analyse est en accord avec les résultats de l'ACC, dans lequel une augmentation de la friction du fond mène à une augmentation du transport de vent thermique (Nadeau & Ferrari, 2015). Cependant, contrairement à l'ACC, aucune étude sur l'intensité du gyre de Beaufort n'a évalué l'effet de la friction de fond en interaction avec des variations de la contrainte de surface.

0.4 Gouverneur océan-glace

L'ACC et le gyre de Beaufort sont tous les deux des courants de hautes latitudes qui partagent une dynamique imposée par le forçage du vent et des tourbillons baroclines. Cependant, l'importance de la couverture de glace les différencie. La couverture de glace de l'ACC ne dépasse pas considérablement le continent antarctique en été (Yuan & Martinson, 2000), donc les études de sa dynamique à grande échelle négligent son effet sur la circulation (e.g. Bai et al. 2021). Dans le gyre de Beaufort, la médiane de 1981 à 2010 de l'étendue de la glace en été couvre presque toute la mer de Beaufort (Timmermans & Toole, 2023). Cette couverture influence la contrainte de surface du gyre, modulant l'intensité du transport d'Ekman via les contraintes internes de la glace, et doit donc être prise en compte dans la dynamique du gyre.

Pour un système avec une couverture de glace, la contrainte à la surface de l'océan, τ, est composée d'un apport de la contrainte de l'atmosphère et d'un apport de la contrainte de la glace :

$$\tau = \alpha C_{Di} \rho_o |\mathbf{u}_i - \mathbf{u}_o| (\mathbf{u}_i - \mathbf{u}_o) + (1 - \alpha) C_{Da} \rho_a |\mathbf{u}_a| \mathbf{u}_a, \tag{3}$$

où α est la concentration de glace ($\alpha \in [0, 1]$), C_{Di} et C_{Da} sont les coefficients de frottement entre la glace et l'océan et l'atmosphère et l'océan, respectivement, ρ_i et ρ_a sont les densités de la glace et de l'atmosphère, et $\mathbf{u}_a$, $\mathbf{u}_i$, $\mathbf{u}_o$ sont les vélocités de l'atmosphère, de la glace et de l'océan. Meneghello et al. (2018) proposent le concept du gouverneur océan-glace, qui suggère que la glace comporte un mécanisme stabilisant plus important que les tourbillons. Dans un cas complètement couvert de glace ($\alpha = 1$), si l'océan et la glace se déplacent à la même vitesse, les contraintes de surface sont nulles et il n'y a pas d'apport de quantité de mouvement au système océanique dû au vent, ce qui stabilise le gyre. L'étude de Meneghello et al. (2018) démontre que, dans un gyre de Beaufort complètement couvert de glace, le gouverneur océan-glace est le principal mécanisme stabilisateur du gyre. Cependant, son étude néglige les tourbillons, omettant ce mécanisme par construction dans la configuration de son modèle numérique. Dans une étude ultérieure, Doddridge et al. (2019), applique l'effet du gouverneur océan-glace tout en appliquant une paramétrisation des tourbillons réaliste pour le gyre, et démontre plutôt que la dynamique du gyre est régie par un équilibre entre trois mécanismes : le vent, les tourbillons et le gouverneur océan-glace.

0.5 Objectifs

Dans cette étude, nous visons à examiner les liens et les différences entre la dynamique du gyre de Beaufort et celle de l'ACC en analysant le rôle et les interactions des paramètres physiques qui sont centraux pour la dynamique de l'ACC, mais qui n'ont pas encore été étudiés systématiquement dans le contexte du gyre de Beaufort. En particulier, nous explorons l'impact sur le transport de vent thermique de :

(i) la contrainte de vent,

(ii) la topographie,
(iii) la circulation de renversement dans les directions radiale et azimutale,
(iv) le frottement de fond.

De plus, nous évaluerons l'impact de la couverture de glace sur les interactions entre ces paramètres physiques et le transport du gyre.

ARTICLE 1

SATURATION TOURBILLONNAIRE DU GYRE DE BEAUFORT

1.1 Résumé en français du premier article

Nous évaluons dans quelle mesure les connaissances issues de la dynamique du Courant circumpolaire antarctique (ACC) peuvent être transposées au gyre de Beaufort (BG). Bien que les deux systèmes présentent des similarités, plusieurs différences majeures doivent être prises en compte. Au-delà de leurs contrastes géométriques, le BG est couvert de glace de mer et les interactions glace-océan influencent fortement sa dynamique. De plus, alors que le gradient du parametre de Coriolis (plan-β) joue un rôle central dans la dynamique de l'ACC, sa variation est faible dans le BG. Le BG est plutôt circonscrit par un bassin topographique qui modifie les contours de vorticité potentielle, pouvant être interprété comme un plan-β effectif. Nos résultats montrent que, bien que la dynamique de l'ACC puisse éclairer la compréhension du BG, le bassin topographique modifie considérablement la sensibitilité du BG à la glace de mer et à la circulation de renversement. Une distinction apparaît entre le rôle de la topographie azimutale (parallèle au le vent), simulant un talus continental, et celui de la topographie radiale (perpendiculaire au vent), simulant une dorsale sous-marine. La topographie azimutale joue un rôle similaire à celui du plan-β: elle stabilise l'écoulement en modifiant la turbulence locale, renforçant ainsi le transport du BG. De l'autre côté, la topographie radiale agit comme une dorsale qui bloque les contours de vorticité, menant à une saturation tourbillonnaire complète du transport. La glace de mer et la circulation de renversement excercent peu d'influence sur le transport en absence de topographie azimutale, mais leur rôle devient considérable lorsqu'elle est présente. L'impact de l'alignement entre la topographie azimutale et les contraintes de surface sur le transport est également examiné.

Cet article, intitulé "*Eddy saturation of the Beaufort Gyre*", fut rédigé par moi-même, avec la supervision et les conseils du professeur Louis-Philippe Nadeau. Comme nous apportons encore les touches finales à certaines simulations, l'article n'a pas encore été soumis pour publication. La soumission se fera à l'extérieur du cadre de ma maîtrise. En tant que première auteur, j'ai fait la recherche sur l'état de l'art en Arctique, configuré le modèle numérique, analysé les résultats et rédigé le texte. Louis-Philippe Nadeau a monté le projet de recherche, conçu le modèle numérique, supervisé les analyses effectuées, et aidé à la correction du texte. Une version abrégée de cet article a été présentée à la conférence *Ocean Sciences Meeting* à Glasgow en février, 2026.

Eddy saturation of the Beaufort Gyre

1.2 Introduction

The Beaufort Gyre (BG) is the dominant large-scale surface circulation feature of the Arctic Ocean's Canada Basin. Forced by the atmospheric Beaufort High, Ekman convergence at the BG surface draws in relatively fresh surface water from the basin boundaries towards its centre. Through this process, freshwater from river runoff, land and sea ice melt, and net precipitation, accumulate in the BG, making it the largest reservoir of freshwater in the Arctic Ocean (Proshutinsky et al., 2009). There is a growing consensus on the key mechanisms governing BG dynamics, and by extension regulating its freshwater content. Wind-driven Ekman pumping steepens isopycnal slopes, deepening the halocline and intensifying rotational transport through the thermal wind relation. Sea ice modulates this surface stress input by decoupling the surface ocean from the wind stress through internal ice stresses. Baroclinic instabilities generated by steep isopycnal slopes form eddies that act to flatten isopycnals, shoal the halocline and reduce transport (Manucharyan & Spall, 2016; Doddridge et al., 2019; Timmermans & Toole, 2023). This balance between wind-driven strengthening and eddy-driven weakening of circulation intensity has been extensively studied in the Southern Ocean's Antarctic Circumpolar Current (ACC). Although similarities between these systems have been acknowledged, links between the two remain unclear given differences in their geometry, surface forcing, and boundary conditions. Building on the extensive understanding of the ACC, this study aims to use the ACC as a framework for investigating BG dynamics.

The ACC is dominated by a three-way zonal momentum balance: (i) input by winds, (ii) downward transfer by interfacial form stress, and (iii) sink by topography. In a flat bottomed channel, friction is the sole momentum sink, and the Rossby deformation radius, L_d, exerts a strong control on channel transport ($T \sim L_d^{1.4}$, where T is thermal wind transport; Nadeau & Ferrari 2015), with additional, but weaker, sensitivities to the background planetary potential vorticity (PV) gradient and wind stress, scaling approximately as $T \sim \beta^{0.65}$ (Gallet &

Ferrari, 2021) and $T \sim \tau^{0.2}$ (Nadeau & Ferrari, 2015). The addition of topography aligned with the wind direction, representing continental slopes, modifies the local background PV, introducing a topographic β-plane and creating a jet over the slope (Thompson, 2010; Stern et al., 2015). A subsurface blocking ridge entirely removes the transport's sensitivity to wind stress—a regime known as eddy saturation, in which eddy activity offsets additional momentum input from wind forcing (Straub, 1993). In this ridge configuration, stronger friction more effectively removes standing meanders, increasing transport (e.g. Nadeau & Ferrari 2015; Marshall et al. 2017). In both flat and ridge configurations, the inclusion of an overturning circulation modulates transport at weak wind forcing (Youngs et al., 2019).

Although the ACC and BG are both high latitude currents that share the dynamical interplay of isopycnal steepening by surface stress and flattening by baroclinic eddies, comparison between the two remains challenging. In ACC literature, isopycnal steepness is typically inferred from variations in zonal transport, whereas BG studies focus on freshwater content and halocline thickness—quantities directly linked to isopycnal slope and transport but less commonly expressed in equivalent dynamical terms. Moreover, physical parameters central to ACC dynamics, such as blocking ridges, overturning circulation and bottom friction, have either not been addressed or not systematically explored in the BG. The BG also differs from the ACC in its extensive ice cover. The ice-ocean governor (Meneghello et al., 2018) proposes a third mechanism for BG intensity regulation. This mechanism builds from the fact that surface stress in the BG is defined by the relative velocities of the surface ocean and sea ice. When sea ice and ocean velocities match, surface stress vanishes, halting Ekman pumping and equilibrating the gyre. BG dynamics would then be regulated by a three-way balance between wind stress, the ice-ocean governor and eddy diffusivity (Doddridge et al., 2019).

In this study, we examine the links and differences between BG and ACC dynamics by systematically investigating the roles and interactions of physical parameters that are central to ACC dynamics but have not yet been addressed in the BG context. We find that bottom topography plays a key role in the BG strength. The presence of a blocking ridge results in complete eddy saturation, whereas the presence of a continental slope (topography in the azimuthal direction) exerts a control on the effect of sea ice coverage and of overturning circulation. A two layer quasigeostrophic (QG) model with varying topography, surface stress and overturning circulation is employed, described in section 1.3. Although idealized, the QG model allows us to isolate effects of different mechanisms and their interactions on the large-scale BG circulation. This approach has an extensive history in the study of ACC dynamics (e.g. Wolff et al. 1991; Straub 1993; Meredith & Hogg 2006; Nadeau & Ferrari 2015; Youngs et al. 2019), and more recently in the study of the BG (Manucharyan & Stewart, 2022). Section 1.4 presents our main results, and section 1.5 summarizes the conclusions.

1.3 Numerical model

The model is based on the two-layer QG PV equations (e.g. Vallis 2017) on an f-plane ($\beta = 0$):

$$\begin{cases} D_t(\nabla^2\psi_1 + F_1(\psi_2 - \psi_1) - \frac{f_0^2}{gH_1}\psi_1) & = -\frac{f_0}{H_1}\mathscr{H} + \frac{\hat{\mathbf{k}}\cdot\nabla\times\boldsymbol{\tau}}{\rho_0 H_1} - A_h\nabla^6\psi_1 \\ D_t(\nabla^2\psi_2 + F_2(\psi_1 - \psi_2) + \frac{f_0}{H_2}h_b) & = \frac{f_0}{H_2}\mathscr{H} - \mathscr{r}\nabla^2\psi_2 - A_h\nabla^6\psi_2, \end{cases} \tag{1.1}$$

where D_t is the material derivative $(\partial_t() + J[\psi, ()])$, ψ_i is the i^{th} layer streamfunction $(i = 1, 2)$, $F_i = \frac{f_0^2}{g' H_i}$, f_0 is the Coriolis parameter, g is the gravitational acceleration, $g' = g\frac{\Delta\rho}{\rho}$ is the reduced gravity, H_1, H_2 are the first and second layer thicknesses, τ is the surface stress field, $\mathscr{H}$ is the overturning circulation, h_b is the bottom topography, $\mathscr{r}$ is the linear bottom drag coefficient, and A_h is a hyperviscosity coefficient. Each simulation is spun up from rest until a statistically steady state is reached. Diagnostics are computed from 50-year time-mean field averages in this steady state.

1.3.1 Model parameters

The model domain has horizontal dimensions $L \times L$, with $L = 3072 \times 10^3$ m. The reduced gravity, g', is chosen such that the deformation radius is 12 km, based on observations of the BG (Zhao & Timmermans, 2015). As the horizontal resolution is 6 km, this choice of deformation radius allows us to be eddy permitting. A summary of model parameters for QG simulations are given in table 1.

Table 1 – Parameter values used in two layer quasigeostrophic model

Parameter	Description	Value
τ	Linear bottom drag	3.47×10^{-7} s^{-1}
H_1	Top layer thickness	666.67 m
H_2	Bottom layer thickness	3333.33 m
f_0	Coriolis frequency	1×10^{-4}s^{-1}
L_d	Rossby deformation radius	12 km
dx	Horizontal resolution	6 km
ρ_0	Ocean reference density	1000 kg m^{-3}
A_h	Hyperviscosity coefficient	5×10^8 m^4 s $^{-1}$

1.3.2 Forcing fields

Three fields exert forcing on the QG model of (1.1): surface stress, overturning circulation and bottom topography (fig. 2). In iceless simulations, the surface stress depends on the wind stress field; otherwise, the ice model provides the forcing. These three forcing fields in addition to the ice model are described in the following subsections.

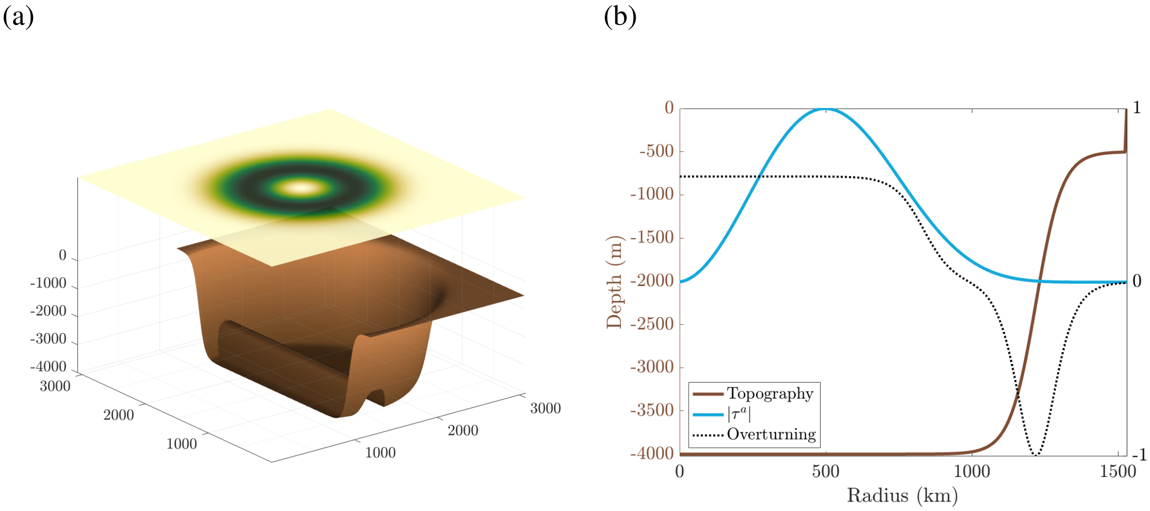

Figure 2 – (a): Three-dimensional model domain. In brown the topographic configuration with both azimuthal and radial components. The depiction of topography is cut off to illustrate the ridge; in practice, the azimuthal topography describes a closed bowl. The yellow to green surface depicts the windstress magnitude field applied at the surface. (b): Cross sections of: azimuthal topography (brown), wind speed (blue) normalized by its maximum value and overturning (black dotted) fields normalized by its maximal absolute value.

1.3.2.1 Surface stress

In an ice-covered ocean, the surface stress, τ can be defined as a sum of a contribution from the atmosphere-ocean stress, $\boldsymbol{\tau}_a$, and a contribution from the ice-ocean stress, $\boldsymbol{\tau}_i$:

$$\tau = \alpha\boldsymbol{\tau}^i + (1-\alpha)\boldsymbol{\tau}^a, \tag{1.2}$$

where α is the ice concentration, taking on a value between 0 (no ice) and 1 (full ice coverage).

When ice is absent, we have $\boldsymbol{\tau} = \boldsymbol{\tau}^q$ with

$$\tau^a = C_{da}\rho_a||\mathbf{u}_a||\mathbf{u}_a, \tag{1.3}$$

where C_{da} is the atmosphere-ocean drag coefficient, ρ_a is the air density, $\mathbf{u}_a$ is the wind velocity, and $\mathbf{u}_1$ is the velocity of the first ocean layer. This formulation does not account for the relative velocity of the top ocean layer with respect to the wind velocity. Additional simulations with this relative velocity formulation showed minimal differences to this simple body-forcing formulation (Appendix I).

When ice concentration is maximal ($\alpha = 1$), we have $\boldsymbol{\tau} = \boldsymbol{\tau}^i$, with

$$\boldsymbol{\tau}^i = C_{di}\rho_i \|\mathbf{u}_i - \mathbf{u}_1\|(\mathbf{u}_i - \mathbf{u}_1), \tag{1.4}$$

where C_{di} is the ice-ocean drag coefficient, ρ_i is the ice density, $\mathbf{u}_i$ is the ice velocity. We use the following parameter values: $C_{da} = 1.3 \times 10^{-3}$, $\rho_a = 1$ kg m^{-3}, $C_{di} = 5.5 \times 10^{-3}$, $\rho_i = 1000$ kg m^{-3}.

The wind velocity imitates an idealized anticylconic Beaufort High (fig. 2), defined by:

$$\begin{cases} u_a = & U_0 \frac{y_0}{r} \cos(\frac{\pi r}{L})^2 \sin(\frac{2\pi r}{L}) \\ v_a = - & U_0 \frac{x_0}{r} \cos(\frac{\pi r}{L})^2 \sin(\frac{2\pi r}{L}), \end{cases} \tag{1.5}$$

where U_0 is the maximal wind magnitude, $(x_0, y_0) = (x, y) - L/2$ are the centered horizontal coordinates and $r = \sqrt{x_0^2 + y_0^2}$ is the radius from the center. The maximal wind magnitude, U_0, is adjusted for each simulation such that the maximum wind stress, τ_0 takes on one of the following values $\{0, 0.001, 0.01, 0.02, 0.05, 0.1, 0.2\}$ N m^{-2}. These values are chosen to cover the parameter space, based off of typical maximal wind stress amplitudes from basin-wide observations of 0.08 Nm $^{-2}$ (Martin et al., 2014).

1.3.2.2 Sea ice

The ice model is defined by a circular slab of constant thickness h_i, rotating about the domain center in solid body rotation. Its angular momentum, ω_i, is constant across the slab and is forced by the wind stress and damped by the ocean:

$$\frac{d\omega_i}{dt} = \frac{1}{I}\left(\int_A r \times \tau^a dA - \int_A r \times \tau^o dA\right), \tag{1.6}$$

where I is the moment of inertia of a cylinder, and τ^o is the quadratic ocean stress. All simulations with the slab ice model have a constant thickness set at $h_i = 1.5$ m, consistent with average sea ice thicknesses observed in the Canada Basin (Kwok, 2018).

1.3.2.3 Topography

Two types of topography are applied, azimuthal topography, simulating a continental slope, and radial topography, simulating a ridge. The azimuthal topography is defined by:

$$h_b = \frac{H_1 + H_2}{2} \tanh\left(\frac{r - R_0}{\mathrm{decay}} + 1\right) \tag{1.7}$$

Where R_0 sets the radius of the central deep basin, and *decay* modulates the steepness of the continental slope. Reference values for these parameters are $R_0 = 1.236 \times 10^6$ m and $decay = 9 \times 10^4$ m, used for all simulations with this topography unless stated otherwise.

The radial topography is constructed from two hyperbolic tangent functions and extends across the entire basin when the bottom is flat, or across the flat-bottomed portion when azimuthal topography is present (fig. 2a). The maximal height of the ridge is 1000m .

1.3.2.4 Overturning circulation

The overturning circulation field aims to simulate downwelling over the shelf regions of the Canada Basin from the subduction of surface waters due to buoyancy fluxes. This field is thus defined by the gradient of the azimuthal-only topography field. We will apply both positive and negative overturning circulations to cover the parameter space. The maximal

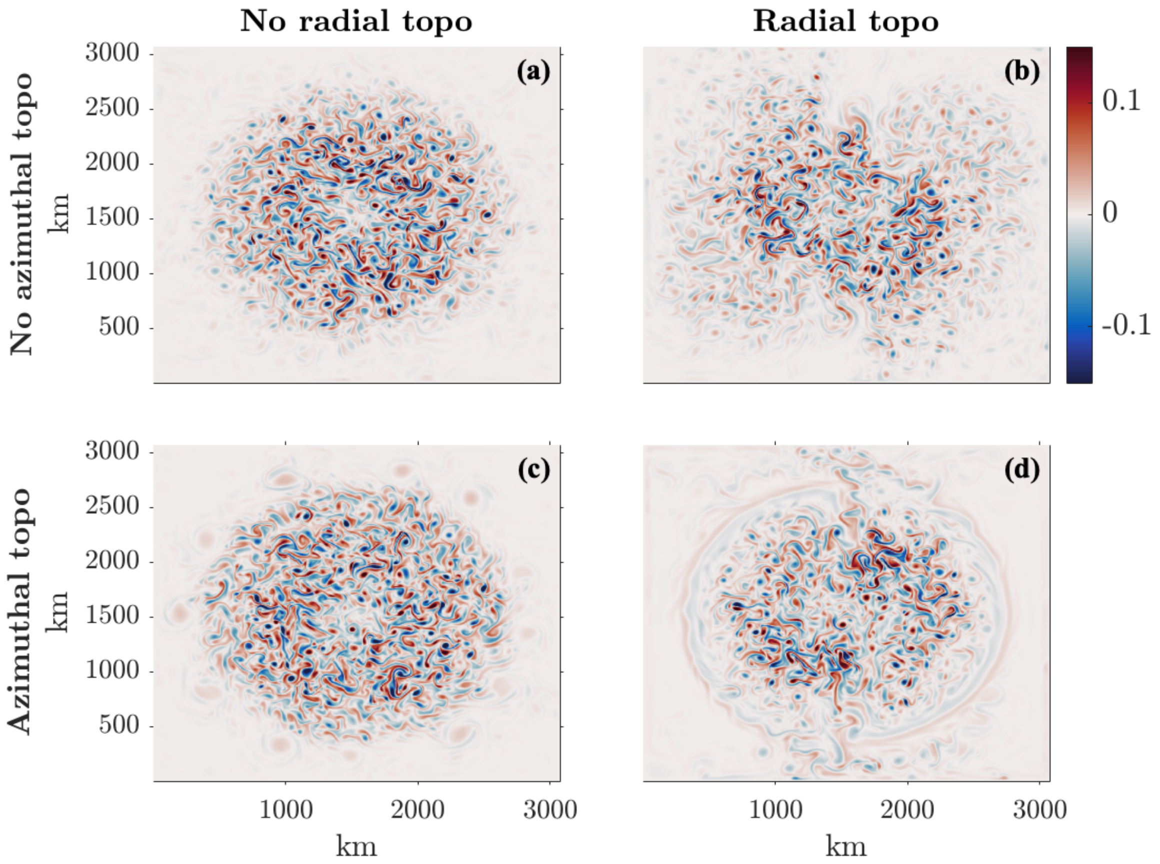

Figure 3 – Snapshots of top layer relative vorticity normalized by the Coriolis parameter (ζ/f_0) of four different topographic configurations. Panels (a) and (b) have no azimuthal topography, whereas (c) and (d) have an azimuthal topographic slope. Panels (b) and (d) have additional radial topography (subsurface ridge). All panels share the same colorbar.

overturning amplitude is applied at the radius where the continental slope is steepest. To ensure that the net vertical transport integrates to zero, a constant upwelling (downwelling) is applied over the flat central region to offset the downwelling (upwelling) over the slopes (fig. 2):

$$\mathscr{H} = \mathscr{H}_0(\nabla h_b + \text{offset}), \tag{1.8}$$

where $\mathscr{H}_0$ sets the diapycnal mixing magnitude. We have adopted the convention that positive $\mathscr{H}_0$ corresponds to downwelling over continental slopes. Each simulation will take on one of the following amplitudes of overturning: $\mathscr{H}_0 \in \{-4, -2, 0, 2, 4\}$ Sv (1 Sv = 1×10^6 m ^{3} s^{-1}).

1.3.3 Diagnostics

1.3.3.1 Thermal wind transport

The thermal wind equation defines a relationship between the isopycnal slopes and the transport. Therefore, to diagnose the steepness of isopycnal slopes, thermal wind transport, also known as baroclinic transport, is widely used in ACC literature (e.g. Youngs et al., 2019): $T_{tw} = H_1 \int_0^{Ly} (\langle \overline{u_1} \rangle - \langle \overline{u_2} \rangle) \mathrm{d}y$, where the angle brackets,$\langle \bullet \rangle$, denote a zonal average, the overbar, $\overline{\bullet}$, denotes a time average, and Ly is the meridional domain length. By treating the gyre as a closed, circular channel, Ly becomes the gyre radius $L/2$, $\langle \bullet \rangle$ becomes an azimuthal average, dy becomes dr, and the horizontal speeds, (u_1, u_2) become azimuthal speeds (u_1^θ, u_2^θ): $T_{tw} = H_1 \int_0^{L/2} (\langle \overline{u_1^\theta} \rangle - \langle \overline{u_2^\theta} \rangle)\, \mathrm{d}r$. Using the fact that $u^\theta = \frac{\partial \psi}{\partial r}$, we can simplify this equation to: $T_{tw} = H_1[((\langle \overline{\psi_1}|_{r=0} \rangle - \langle \overline{\psi_2}|_{r=0} \rangle)) - \langle \overline{\psi_1}|_{r=L/2} \rangle - \langle \overline{\psi_2}|_{r=L/2} \rangle))]$. Where at $r = 0$, the azimuthal average of a field reduces to the field's value at the center. We further approximate that the value of both layers' streamfunctions azimuthal mean at $r = L/2$ is equal to the value at the western border. Since the streamfunction at $r = L/2$ in both layers is usually very close to zero, values of transport using the azimuthal mean method versus the western border method yield virtually identical results. We can thus drop the angle brackets and obtain:

$$T_{tw} = H_1[(\overline{\psi_1^{edge}} - \overline{\psi_2^{edge}}) - (\overline{\psi_1^{mid}} - \overline{\psi_2^{mid}})], \tag{1.9}$$

where *mid* and *edge* superscripts denote field values at the center and the western border, respectively.

We have decided to use a metric for isopycnal slope steepness that is widely used in ACC literature. However, thermal wind transport is not commonly used to describe circulation strength in the BG. Since the most prominent feature of the BG is its strong freshwater content, studies commonly use metrics that more directly reflect the halocline thickness, with the choice depending on the numerical model employed. Examples include the sea surface height in the center of the basin (Lique et al., 2015), the halocline depth at the center of the domain (Yang et al., 2016), the asymptotic halocline depth anomaly (Meneghello et al., 2018; Doddridge et al., 2019), the freshwater content computed from vertically integrated salinity relative to a reference salinity (Manucharyan & Spall, 2016; Manucharyan et al., 2017; Manucharyan & Isachsen, 2019), and the gyre-wide halocline deepening (Manucharyan et al., 2016). Despite the focus on thermal wind transport in the ACC and on halocline in the BG, these two properties are closely related. In two-layer QG in the BG configuration, halocline depth anomaly, h, can be defined by the maximal depth of the interface between the two layers: $\eta_1 = \frac{f_0}{g'}(\psi_2 - \psi_1)$. The maximal value for the time mean streamfunctions of both layers in the gyre geometry is at its center, giving:

$$h = \frac{f_0}{g'}(\psi_2^{mid} - \psi_1^{mid}). \tag{1.10}$$

Plugging in the expression for T_{tw}, we obtain $h = -\frac{f_0}{g'}(\frac{T_{tw}}{H_1} + (\psi_1^{edge} - \psi_2^{edge}))$. Where, in our configuration, there is very little forcing near the domain edges, leading to streamfunction values that are close to zero there. We use the following approximation to express the relationship between thermal wind transport and halocline depth anomaly:

$$h \approx -\frac{f_0}{g' H_1} T_{tw} \tag{1.11}$$

1.3.3.2 Eddy kinetic energy

The total eddy kinetic energy is computed using time-mean speed fields, $(\overline{u}, \overline{v})$, and time-mean kinetic energy fields ($\overline{KE} = \overline{u^2 + v^2}$):

$$\overline{EKE} = H_1(\overline{KE}_1 - (\overline{u_1}^2 + \overline{v_1}^2)) + H_2(\overline{KE}_2 - (\overline{u_2}^2 + \overline{v_2}^2)). \tag{1.12}$$

1.4 Results

1.4.1 Radial Topography

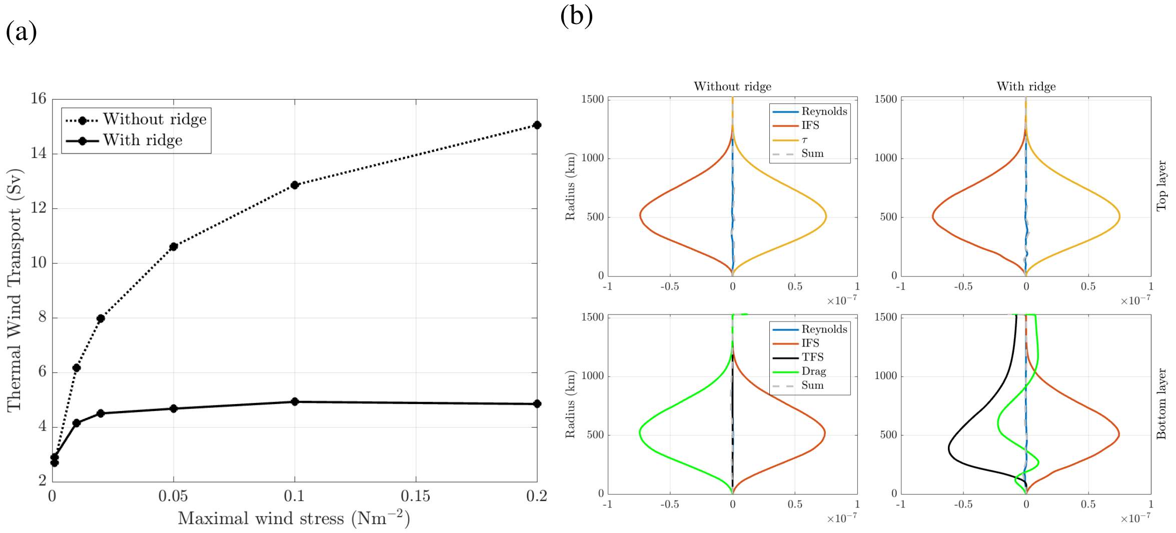

Figure 4 – (a): Flat bottom (dotted curve) and ridge bottom (solid curve) thermal wind transports at various maximal wind stresses when no azimuthal topography is applied. (b): Momentum budget of top layer (top row) and bottom layer (bottom row) for flat case (left column) and for ridge case (right column) at $\tau_0 = 0.05\text{Nm}^{-2}$. Interfacial form stress is abbreviated as IFS and topographic form stress as TFS.

We first explore the effect of radial topography in the form of a ridge, in the absence of azimuthal topography (fig. 3 a and b). In the completely flat bottomed case, thermal wind transport increases sub-linearly with respect to wind stress (fig. 4a). We observe an approximate relationship of $T_{tw} \sim \tau^{0.3}$, which sits in between the cube-root dependence in the BG found by Manucharyan & Spall (2016) and the $T_{tw} \sim \tau^{0.2}$ relationship observed in ACC (Nadeau & Ferrari, 2015). In both ridgeless and ridge cases, momentum is input by the wind stress, transferred from the first layer to the second via interfacial form stresses (IFS), and the momentum is dissipated by the bottom topography (fig. 4b), consistent with the ACC momentum budget. The momentum sink in the ridgeless case is bottom drag, whereas when the ridge is added, bottom drag is an order of magnitude less important, and topographic form stress (TFS) accounts for the majority of the momentum sink. At weak wind stresses, the thermal wind transport of ridge and ridgeless configurations converges. With the presence of the ridge, a completely saturated regime emerges. This has never been explored in the BG, but is concurrent with ACC litterature (e.g. Hallberg & Gnanadesikan 2001; Nadeau & Straub 2012; Youngs et al. 2019). We note that although we use a blocking ridge that spans the width of the domain, anywhere from a half-ridge to a full ridge produces saturation (Appendix II, fig. 15).

1.4.2 Azimuthal Topography

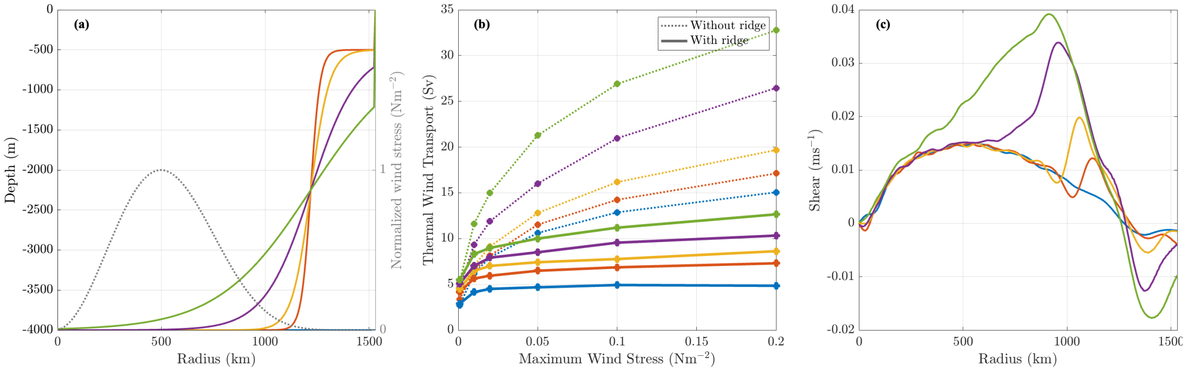

Figure 5 – (a): Bottom topographies of various azimuthal topographic slopes (solid colored curves) with normalized wind stress plotted for reference (black dotted curve). Max slope steepness values are elements of $\{0, 0.004, 0.008, 0.02, 0.04\}$. (b): Thermal wind transport of various slopes at various wind stresses with (solid curves) and without (dotted curves) a ridge. (c): Cross-section of vertical shear of various azimuthal topographic slopes at $\tau_0 = 0.05$ Nm^{-2}.

Here, we vary the slope of the azimuthal topography to determine its effect on the BG transport. Four slopes of varying steepness are applied (fig. 5a), where we note that in QG theory only the gradient of topography affects the dynamics, therefore the altered shelf depths associated to different slope steepness do not affect the results. Varying the slope affects the thermal wind transport magnitudes, but does not alter the $T_{tw} \sim \tau^{0.3}$ power law relationship observed in figure 4a where azimuthal topography is absent. Eddy saturation is maintained in ridge configurations, with a slight loss of complete saturation for shallower topographic slopes, attributed to the reduction in blocked PV contours by the ridge as the slope flattens. Our initial prediction on the effect of the azimuthal topographic slope is that steeper slopes would increase transport. This rationale is based on the fact that a slope introduces a topographic β, relaxing the baroclinic instability criterion locally, reducing eddy generation. Thus, a steeper slope would produce a stronger topographic β and more effectively limit eddy activity, increasing transport (Appendix II, fig. 16). However, what we observe (fig. 5b) is the opposite: as slope steepness weakens, transport increases. We attribute this result to two effects. First off, the weaker slopes are also much wider than the steep slopes. Thus, as the topographic slope flattens, the topographic β–albeit weaker–is applied to a wider region. The time mean vertical shear illustrates this; when there is no topographic slope, no jet forms over the shelf break, but when we add the slope, the jet appears and widens as the slope flattens (fig. 5c). A weaker eddy activity is observable over the continental slope region in the vorticity snapshots of simulations with azimuthal topography in comparison to those without it (fig. 3). This finding is consistent with results from Manucharyan & Isachsen (2019), who showed that, when slope steepness is held constant, wider slopes generate wider and stronger jets, increasing transport.

We additionally note that as slope width increases (and slope steepness decreases), the vertical shear migrates towards the center of the domain, and increases its maximal value. We attribute this to the second effect of varying slope steepness: the alignment of topography with the wind stress. Additional simulations with fixed slope steepness but varying distance of the slope from the wind stress maximum demonstrate this (fig. 6). When the slope and wind stress are in closer alignment, the jet strength maximum migrates towards the steepness maximum but also increases in strength. Therefore in our continental slope steepness experiments (fig. 5), since flatter slopes are wider, there is more sloped topography where the wind stress is stronger, increasing transport.

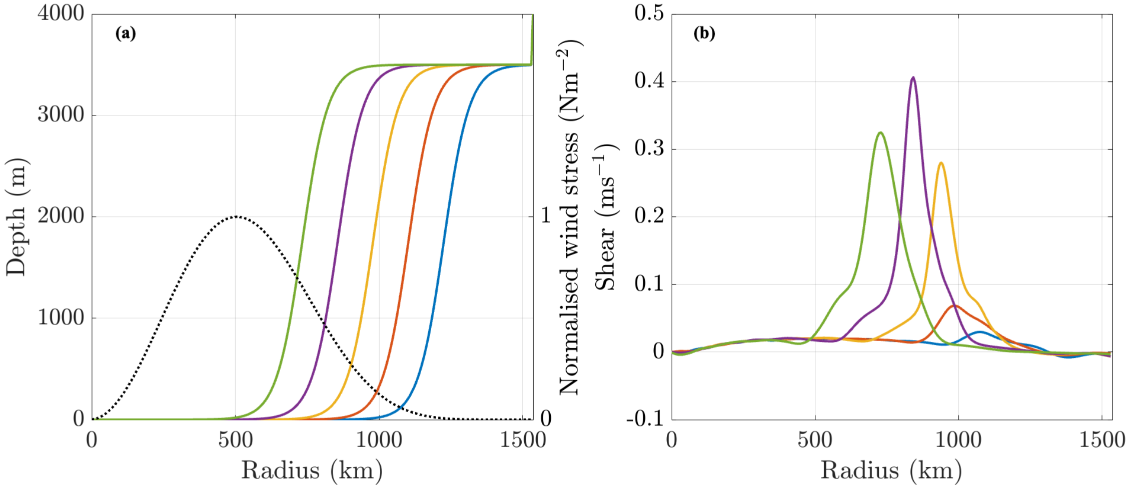

Figure 6 – (a) Topography (coloured, solid curves) of simulations with a varying distance of the continental slope to the domain center. Distance of the max slope steepness to the center varies from 1226 km (green curve) to 738 km (blue curve). The reference bowl topography referenced in the rest of the manuscript is the green curve. The dotted black line is the normalized wind stress. (b) Time mean vertical shear of the varying slope distance simulations. All simulations have a maximum wind stress of $\tau_0 = 0.05$ Nm $^{-2}$.

For the remainder of the manuscript we will use the second slope (fig. 5, yellow curve) for comparing configurations with and without azimuthal topography.

1.4.3 Sea ice

Including a slab ice in the surface forcing of the first ocean layer does not considerably affect the thermal wind transport when no azimuthal topography is present, although there is an increased thermal wind transport at all wind stresses (fig. 7a), which we attribute to eddy killing. However, when the azimuthal topography is included, transport in the ice-covered simulations becomes markedly larger than in the iceless case (fig. 7b). Comparing vorticity snapshots, it is clear that eddies are much weaker in the ice-covered configurations that the iceless ones (fig. 3 vs. fig. 8, note differing colorbars). Despite the eddy kinetic energy (EKE) being much weaker in ice-covered simulations, this EKE reduction cannot explain the differing behaviour that emerges when slab ice is combined with the azimuthal topography

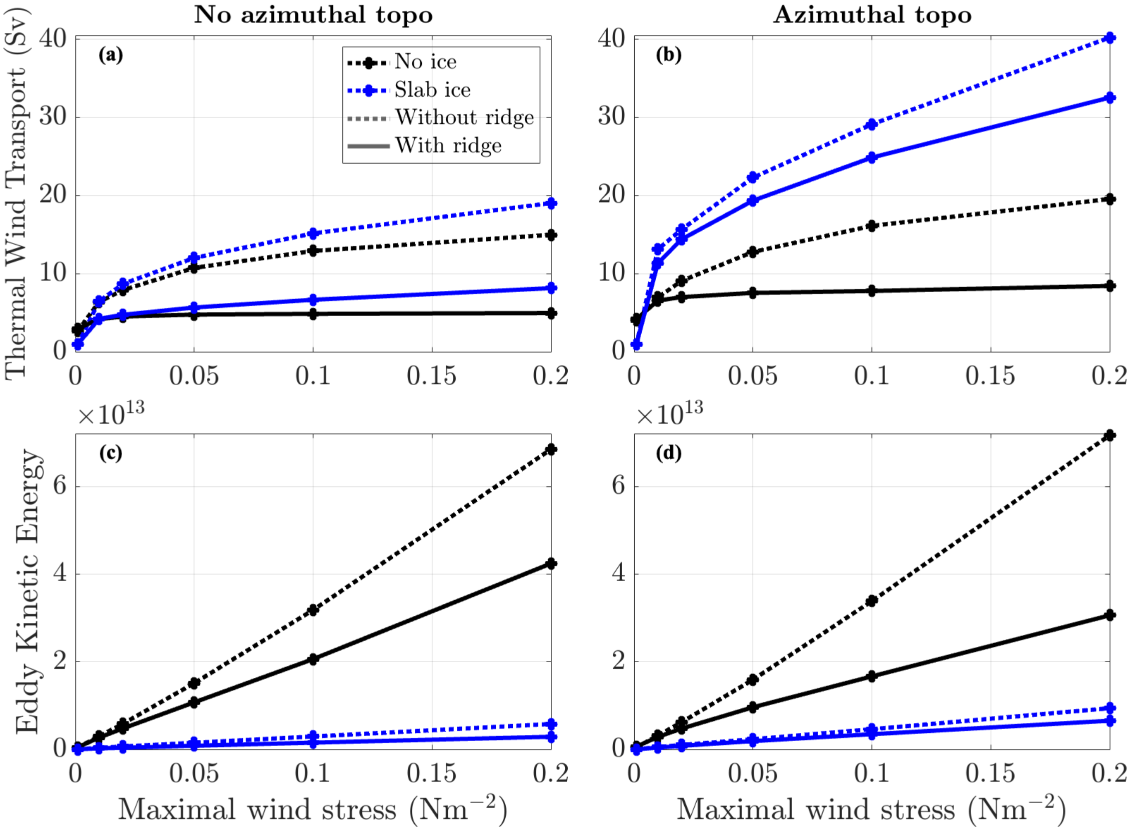

Figure 7 – Thermal wind transport (a, b) and eddy kinetic energy (c,d) of simulations without (black curve) and with (blue curve) slab ice for simulations either (a) without azimuthal topography or (b) with azimuthal topography (yellow curve in figure 5). Simulations with ridgeless topography is denoted by the dotted curves, ridge topography by the solid curves.

(fig. 7c, 7d), since it occurs in configurations both with and without this topographic feature. Instead, we attribute the striking increase in transport to the alignment between the surface stress and the azimuthal topography. In the iceless case, the maximal wind stress and azimuthal topographic slope are not well aligned, since the topographic slope is about 300km from the edge of the domain, where wind stress is close to zero (fig. 9d). When ice coverage is applied, the slab redistributes the wind stress over the ice disk, applying maximal surface stress at a radius of $L/2$. The surface stress and topography are therefore much more aligned than in the iceless case, explaining the marked increase in transport.

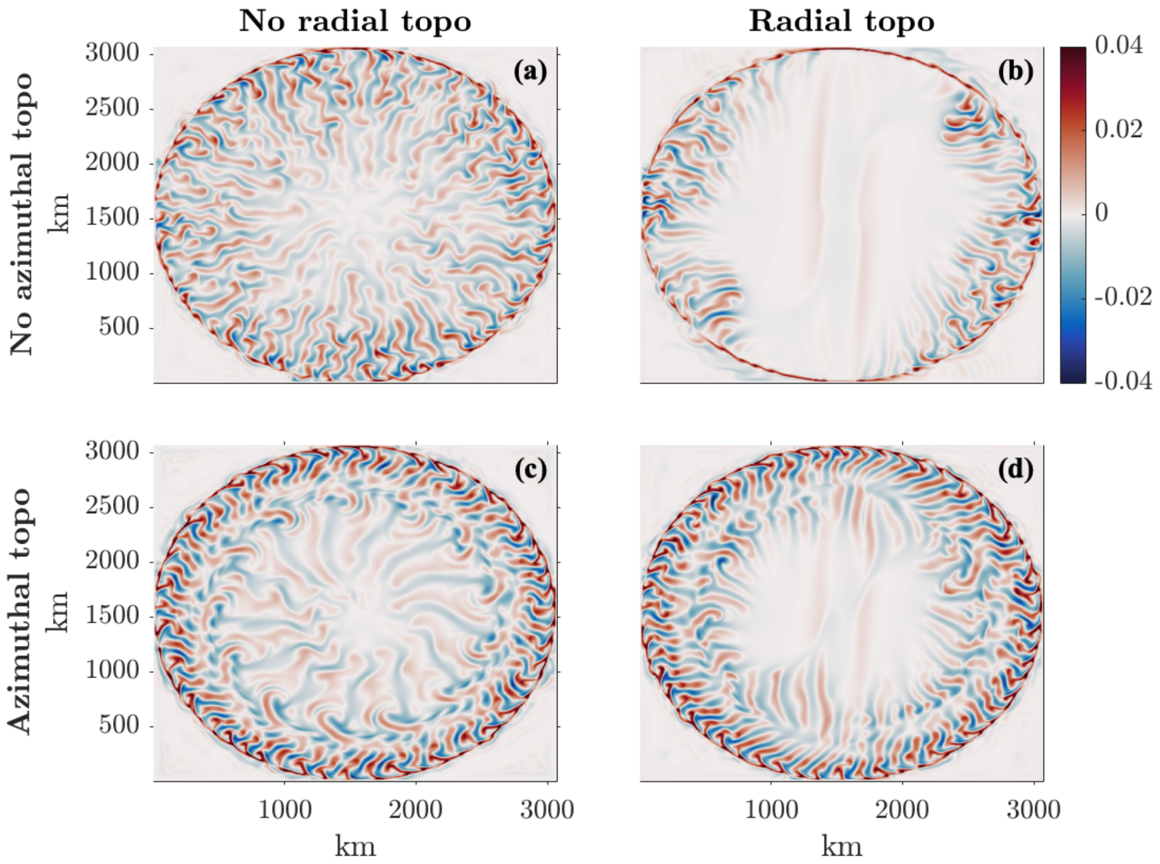

Figure 8 – Snapshots of ocean top layer relative vorticity normalized by the Coriolis parameter (ζ/f_0) of simulations with ice coverage with four different topographic configurations. Panels (a) and (b) have no azimuthal topography, whereas (c) and (d) have an azimuthal topographic slope. Panels (b) and (d) have additional radial topography in the form of a subsurface ridge. All panels share the same colorbar. Note the colorbar differs from snapshots of iceless simulations (fig. 3).

These results invite comparison with what has been termed the ice–ocean governor. According to this proposed mechanism, under strong ice coverage the ocean speed and ice speed are virtually matched, driving surface stress toward zero, equilibrating the gyre (Meneghello et al., 2018). When azimuthal topography is absent, the surface stress of the ice-covered case, although much weaker than the iceless configuration, is not zero (fig. 9c). It increases linearly with increasing radius, coherent with the solid-body rotation of the ice. When azimuthal topography is applied, the surface stress increases linearly with radius in the central,

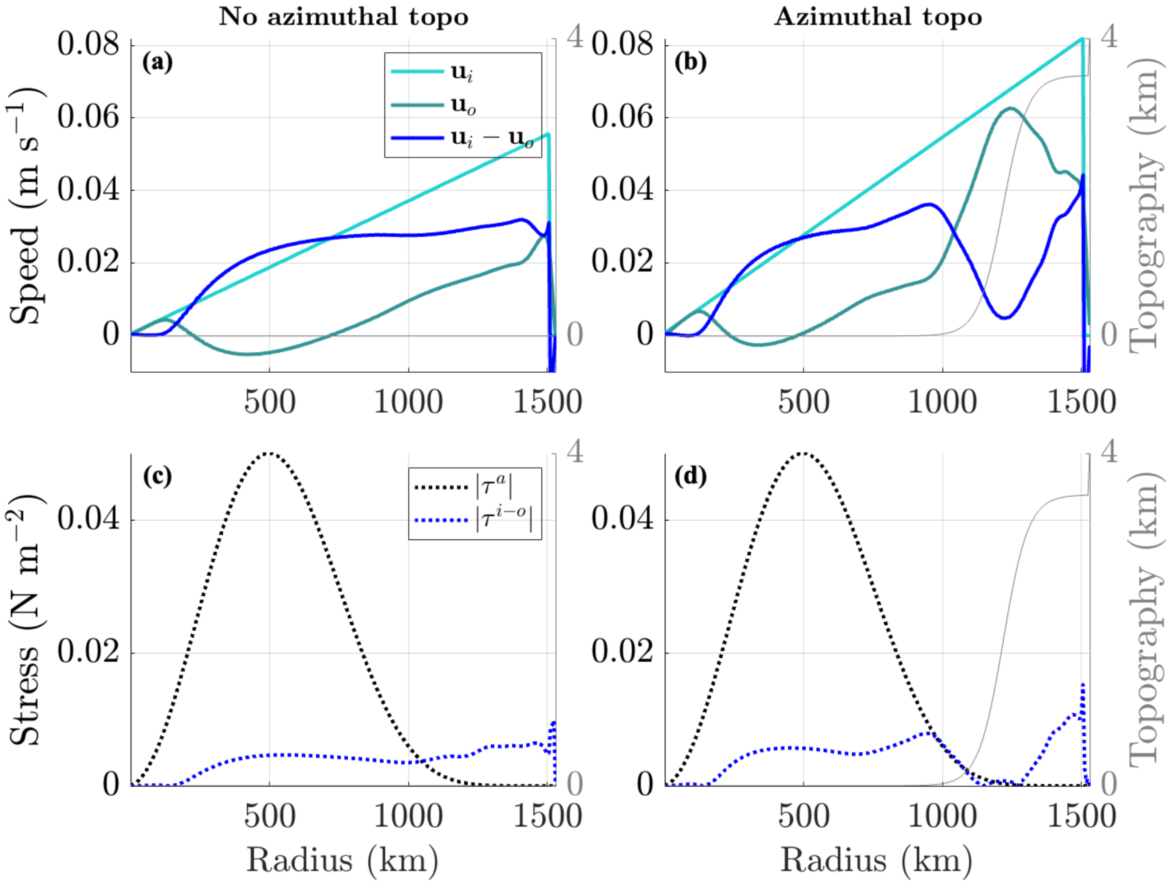

Figure 9 – Top: time-mean, azimuthally averaged ice (cyan), ocean (teal) and ice minus ocean (blue) speeds. Bottom: time-mean, azimuthally averaged atmospheric stress (black dotted) and ice-ocean stress (dotted blue). Bottom topography is represented by the thin grey curve in all panels.

flat-bottomed portion of the bowl-like topography (fig. 9d). Once the bottom topography begins to slope ($r \sim 1000$ km), vertical shear increases, indicating strong surface circulation consistent with a slope jet. This maximum in vertical shear is aligned with both a maximum topographic slope, and a surface stress that falls to zero. Over the continental shelf region, shear decreases and surface stress returns to values consistent with the solid body rotation of the slab. The governor effect appears to apply to the continental slope region, where ocean speeds are strong enough to match ice speeds and effectively turn off the surface stress. However, this effect appears to be a local one. The relationship between global (spatially averaged) ice and ocean speeds is linear, but the ocean speed is about 40% smaller than the ice speed (fig. 10a), indicating that, on average, surface stress continues to input momentum into the system.

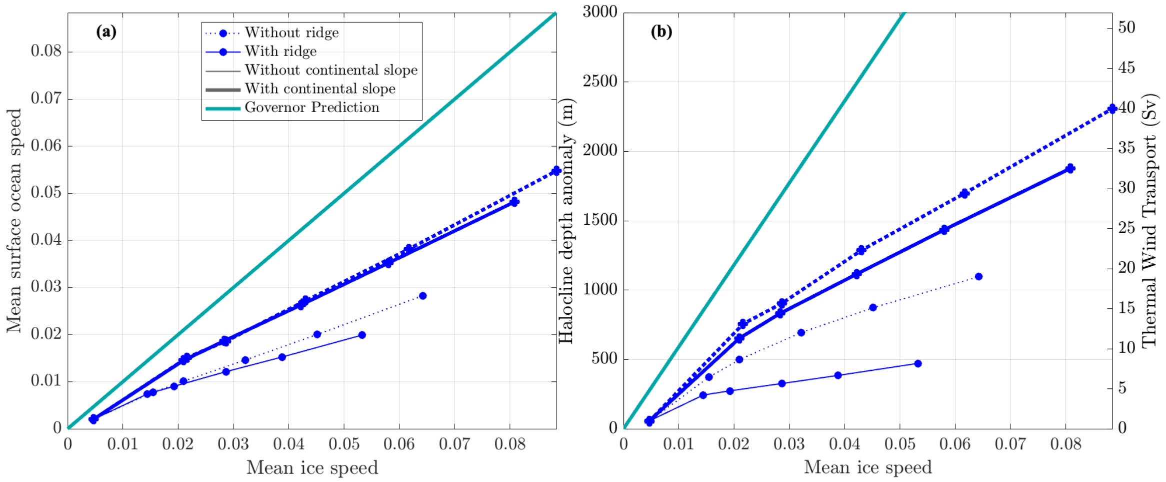

Figure 10 – (a): Average ocean surface layer speed versus average slab ice speed for configurations without a ridge (dotted curves), with a ridge (solid curves), without azimuthal topography (thinner curves) and with azimuthal topography (thicker curves). Solid cyan line represents the one-to-one ratio. (b): Halocline depth anomaly (left y axis) and equivalent thermal wind transport using 1.11 (right y axis) versus mean ice speed for slab ice simulations. Curve line-styles represent the same configurations as in (a). The cyan curve represents the predicted halocline depth anomaly and associated thermal wind transport using the limiting governor case as in Doddridge et al. (2019).

Doddridge et al. (2019) proposed a differential equation for determining the halocline depth anomaly from wind stress, ice speed and eddy diffusivity. In the limiting case of a full ice-ocean governor ($u_i = u_1$), with zero eddy diffusivity and complete ice coverage, they obtain a relationship solely dependant on ice speed: $h = \frac{u_i f_0 R}{g'}$, where R is the radius of the gyre. We compare our slab ice findings with this deterministic relationship (fig. 10b), using the parameters: $R = L/2$ m, $f_0 = 1\times10^{-4}$ s^{-1}, $g' = 2.6\times10^{-3}$ m s^{-2}. We find that even with the slab-ice model in solid-body rotation, our resulting halocline depth anomaly (and equivalently thermal wind transport) remains below the governor prediction. This departure likely arises from (i) turbulence, which the governor limit explicitly neglects, and (ii) ocean speeds being, on average, weaker than ice speeds in our results. Our ice-covered simulations most closely ressemble the ice-ocean governor prediction when azimuthal, ridgeless topography is applied. Our results show that, despite the eddy killing introduced by the ice, eddies exert a non-negligible control on transport—even under a thick, consolidated ice pack.

1.4.4 Overturning circulation

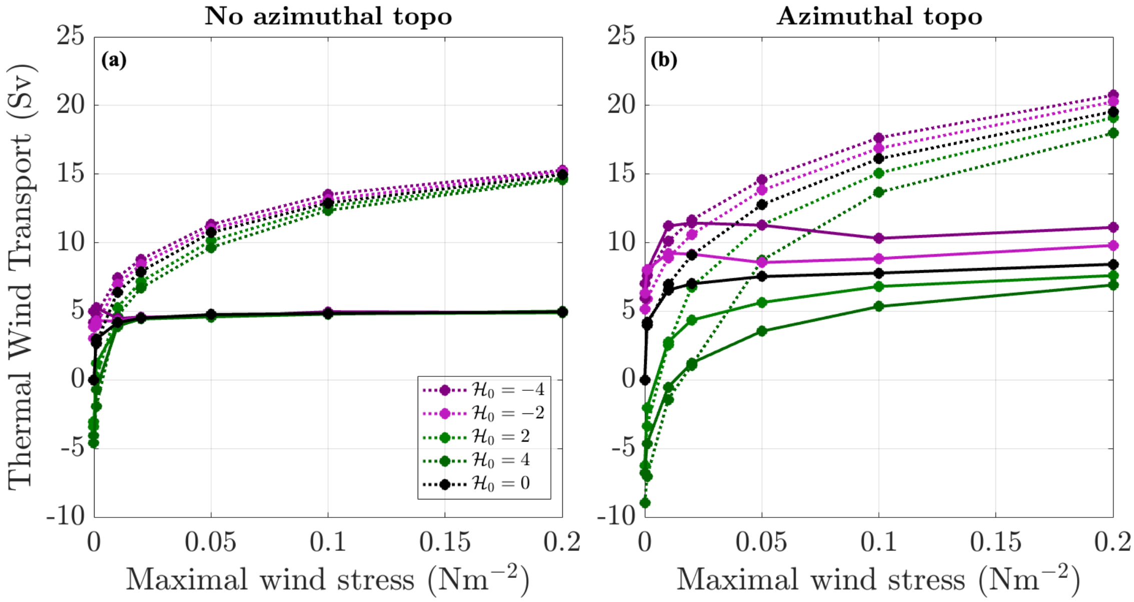

Figure 11 – (a): Thermal wind transport for simulations without azimuthal topography either without (dotted curves) or with (solid curves) ridge. Different curve colours represent different overturning circulation magnitudes. Positive overturning corresponds to downwelling over the azimuthal topographic slope and negative overturning to upwelling. (b): same as (a) but with azimuthal topography.

Applying an overturning circulation has a negligible impact on thermal wind transport in the configurations without azimuthal topography (fig. 11a), but its effect becomes evident when azimuthal topography is included (fig. 11b). We attribute this to the stabilizing effect of the topographic β introduced by the continental slope. Since the overturning circulation field is maximal where the topographic slope is steepest, we are forcing at the location where the baroclinic instability criterion is the most relaxed. As a result, turbulence is reduced at the location of the imposed overturning, making the thermal wind transport more sensitive to changes in the overturning strength when azimuthal topography is present.

In the case with azimuthal topography, we observe a stronger dependence on overturning at weaker wind stresses, with thermal wind transport beginning to converge at high wind stresses. At weak wind stress, the isopycnal slopes are more sensitive to overturning since eddy kinetic energy is weaker. These results are similar to what Youngs et al. (2019) found in their study on overturning circulation in the ACC (c.f. their figure 4). However their study used a β-plane, as is customary in ACC configurations, and did not include azimuthal topography. This suggests a dynamical parallel between ACC sensitivity to overturning on a β-plane and BG sensitivity to overturning on an f-plane with topographic β.

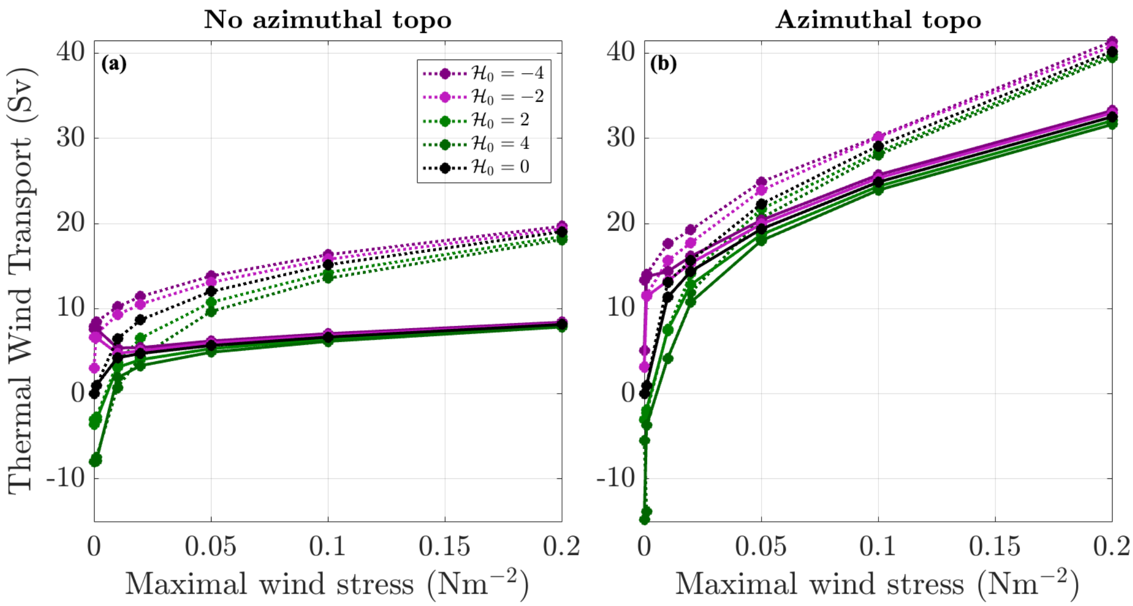

Figure 12 – Same as figure 11 for ice-covered simulations.

Simulations with the slab ice show sensitivity to overturning both with and without azimuthal topography (fig. 12). In the case with a ridge and without azimuthal topography, thermal wind transport is especially sensitive to overturning at wind stresses weaker than 0.05 N m^{-2}, above which transport converges to the $\mathscr{H}_0$ = 0 Sv value. In the case with azimuthal topography, the effect of overturning is relatively constant at all wind stresses, regardless of the presence or absence of a ridge. The emergence of a sensitivity to overturning in ice-covered versus iceless simulations highlights the important role of eddies in the iceless runs, especially in configurations without azimuthal topography. A stronger eddy energy field in iceless configurations, as seen in the snapshots of vorticity (fig. 3 vs. 8), and in the mean EKE values (fig. 7c) leads to a reduced effect of the overturning on iceless simulations in the absence of azimuthal topography. In contrast, a weak eddy energy field in the ice-covered simulations allows the overturning circulation to play a role in transport magnitude.

1.4.5 Bottom drag

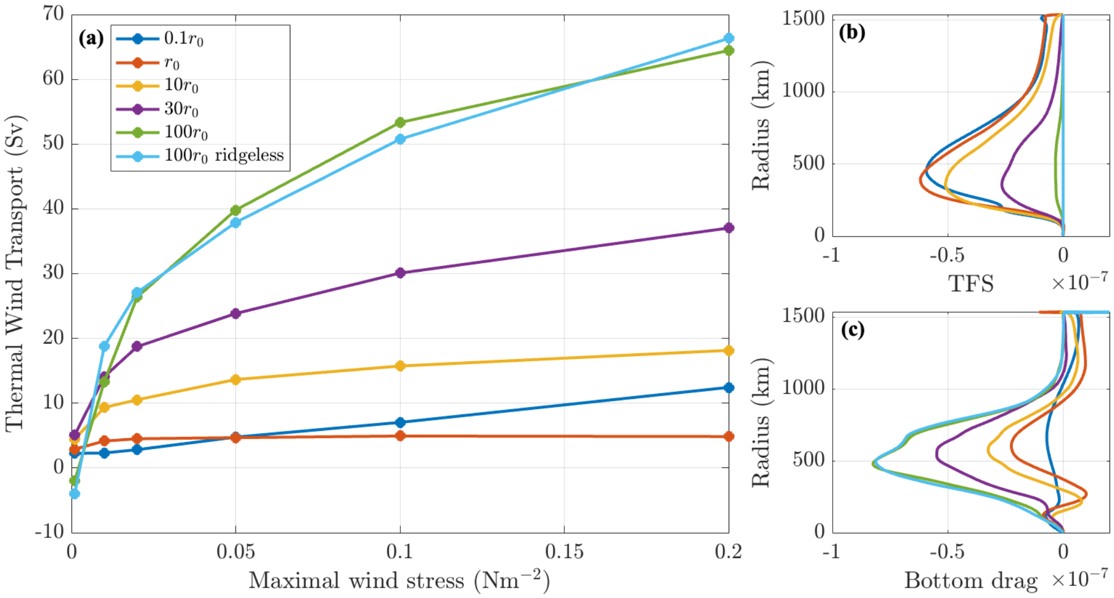

Figure 13 – (a): Thermal wind transport of simulations without azimuthal topography and with a ridge (unless otherwise stated in the legend) with various bottom drag coefficients. (b): Topographic form stress (TFS) momentum sink of simulations in (a). (c): Bottom drag momentum sink of simulations in (a).

We explore the effect of bottom drag on the configuration without azimuthal topography and with a ridge. When the bottom drag coefficient is increased from our reference value,

r_0, by a factor of 10, thermal wind transport increases and complete saturation is lost (fig. 13a). An increase by a factor of 100 produces an even stronger transport and greater loss of saturation. These results are consistent with findings from the ACC, where increased bottom drag induces a similar increase in transport and reduced saturation (Nadeau & Straub, 2012). This behavior can be explained by a shift in the principal momentum sink from topographic form stress to bottom friction (fig. 13b, 13c). At $r = 100r_0$, thermal wind transport values converge for various bottom topographies: ridge without azimuthal topography, ridge with azimuthal topography, and azimuthal topography without ridge. Strong friction coefficients thus completely render the thermal wind transport insensitive to bottom topographic features. Explorations on r in the ACC also find a convergence of the thermal wind transports of various topographies at high bottom drags (Nadeau & Ferrari, 2015).

We highlight that, although the use of a sufficiently small bottom drag coefficient is necessary for topographic form stress to impact the momentum budget, smaller coefficients also lead to longer equilibration time scales. Our simulations with $r = r_0$ took roughly 10 times longer to converge than the $r = 100r_0$ ones (~1000 years versus ~100). The choice of a bottom friction parameter therefore not only impacts the momentum budget, but also the numerical feasibility of simulations. Past idealized studies of the BG have employed comparatively large bottom drag coefficients, although most use quadratic drag, making direct comparison with our linear formulation less straightforward. Arbic & Scott (2008) suggest a non-dimensional friction strength parameter, defined for both linear and quadratic drag, for which observational estimates suggest values of order 1. The friction strength parameter in our study with $r = r_0$ is 0.45. In contrast, various idealized BG studies adopt quadratic drag coefficients on the order of 1×10^{-2} , corresponding to friction strengths of order 100, similar to our $r = 100r_0$ simulations, effectively suppressing the topographic form-stress momentum sink.

1.5 Conclusion

We investigate the potential for eddy saturation in the BG and explore physical processes that modulate it. Although eddy saturation is a well-established feature of the ACC (e.g., Straub 1993; Nadeau & Straub 2012; Nadeau & Ferrari 2015; Marshall et al. 2017; Youngs et al. 2019), it has never been explicitly examined in the BG, despite the dynamical similarities between the two systems. We show that an eddy-saturated state does arise in an idealized BG configuration when a blocking ridge is present in the bottom topography, regardless of whether azimuthal topography is present. We find that the azimuthal topography exerts a control on how sea-ice and overturning circulation affect the gyre transport: in the absence of a slope, neither process influences the BG intensity, but when the slope is present they both become relevant. Finally, we demonstrate that bottom drag strongly modulates the dominant momentum sink. For weak drag, topographic form stress is the principal sink, whereas increasing the bottom drag coefficient shifts the balance toward bottom friction as a momentum sink and renders the system increasingly insensitive to the underlying topography.

The presence of a continental slope in the form of azimuthal topography is known to suppress eddy activity in the BG, ultimately increasing transport (Manucharyan & Isachsen, 2019; Isachsen et al., 2024). The slope introduces a topographic β, relaxing the baroclinic instability criterion locally, reducing turbulence and leading to the emergence of a slope jet (fig. 5c). We show that the interaction of the azimuthal topographic slope's stabilizing effect coupled with ice coverage or overturning circulation vastly impacts the response of the BG transport. We find that improved alignment between the surface stress and the slope steepness maximum increases transport considerably. The slab ice redistributes wind stress such that surface stress is more aligned with the azimuthal topography, substantially increasing transport and reducing saturation. The overturning circulation is, by construction, maximal where the topographic slope is steepest, and thus plays a key role in setting the transport when the slope is present, especially at low wind stresses. Our findings contrast with ACC results, where the effect of sloping topography has a more limited effect on the system's response (e.g. Bai et al. 2021; Thompson 2010). This could be explained by an attenuation of the local effect of a sloping topography by the background PV imposed by the β-plane. In the BG, the f-plane configuration leads to a higher sensitivity to the stabilizing effect of the azimuthal topographic slope on the circulation. An analogy can be made between the ACC's β-plane and the BG topographic β introduced by the azimuthal topographic slope, which can particularly be observed in the similarities between our overturning circulation results (fig. 11bc), and those conducted in the ACC (Youngs et al. 2019, fig. 4). However, although both planetary and topographic β stabilize the circulation by suppressing turbulence, the topographic β has been shown to barotropize turbulent energy at large scales, whereas planetary β is neutral in the conversion between barotropic and baroclinic modes (Deng & Wang, 2024). More work is required to understand how the difference in conversion between modes impacts the response to overturning in ACC versus in BG configurations.

The ice-ocean governor is discussed in BG dynamics as a mechanism by which surface stress tends to zero, shutting off Ekman pumping, and stabilizing the gyre (Meneghello et al., 2018). Here, we use a disk of constant thickness in solid body rotation, simulating a strong winter sea ice pack to determine if the system approaches the governor limit. We found that it is the redistribution of surface forcing over continental slopes, rather than the presence or absence of ice coverage, that determines the response of the system. Surface ocean speeds are consistently lower than ice speeds (fig. 10a), only locally attaining the zero relative speed fundamental to the governor (fig. 9d). The pure governor prediction over-estimates thermal wind transport in our ice-covered simulations (fig. 10b), highlighting that eddies continue to play a role in BG dynamics, even under winter ice coverage. This is concurrent with findings from Mason & Smith (2025), who explored two sea ice limits in the BG, a motile ice and a static ice, and found that, although eddy energy is stronger under motile ice, it remains substantial even under static ice. In light of both their results and our findings, the presence of sea ice in the BG does not appear to act as a distinct dynamical control, but rather to spatially redistribute surface momentum input and modulate its magnitude.

There are limitations to the idealized nature of our configuration. The two-layer QG framework assumes small interface displacements, and the QGPV approximation becomes less robust when eddies interact strongly with steep topography. A primitive-equation model would be valuable for assessing the robustness of the mechanisms identified here. In addition, our geometry is a simplified representation of the BG. In reality, the BG topography is somewhere in between the configurations with and without azimuthal topography. The ridge is also a simplification of the complex BG bottom topography. We show that complete saturation can occur for ridges that span at least half the domain, independent of the presence or absence of azimuthal topography. The gyre is known to periodically extend over the Northwind Ridge (Regan et al., 2019), supporting the relevance of a partial blocking ridge, although the orientation of this ridge is not exactly matched in our configuration. Finally, our ice model represents a limit of strong, winter sea ice cover and does not represent free-moving ice floes characteristic of summer ice coverage and marginal ice zones, nor does it account for landfast ice and ice friction with the continent. We believe the true surface stress of the BG is defined by a forcing situated somewhere between our ice disk in solid body rotation and our iceless configurations. Despite the lack of realism in our study, our idealized configuration allowed us to identify key contributors to BG strength and to draw dynamical parallels to idealized ACC studies.

We demonstrate that clear links exist between the BG and the ACC, through their momentum budgets, the production of eddy saturation, and sensitivity to bottom friction and overturning circulation. Despite these parallels, the negligible β-plane and redistribution of surface stress by sea ice distinguish the BG from its southern counterpart. Our results show that azimuthal topography exerts a strong control on BG thermal wind transport, highlighting the importance of alignment between topographic slopes and forcing in setting the system's response. These findings point to several open questions that warrant further investigation. Assessing the robustness of these mechanisms in a primitive-equation framework would help confirm how strongly topography affects saturation. Likewise, incorporating more realistic BG characteristics, such as partial ridges, varying azimuthal slopes, and a realistic sea ice model, would strengthen the connection between our idealized results and observations.

CONCLUSION GÉNÉRALE

Ce travail avait pour objectif de mieux comprendre les mécanismes qui gouvernent la variabilité et la réponse dynamique du gyre de Beaufort. En s'appuyant sur une configuration idéalisée inspirée de travaux menés sur le Courant Circumpolaire Antarctique (ACC), nous avons mis en évidence plusieurs processus clés qui structurent la circulation et déterminent sa sensibilité aux contraintes de surface : la saturation tourbillonnaire en présence de topographie radiale, le contrôle de la topographie azimutale sur l'effet du renversement et de la glace, l'amplification du transport due à l'alignement de la topographie avec les contraintes de surface, ainsi que l'attenuation du TFS par la friction de fond. L'ensemble des résultats présentés contribue à établir des parallèles entre la dynamique de ces deux systèmes, tout en soulignant les particularités qui les distinguent, notamment l'absence d'un plan-β et le rôle de la glace de mer dans la redistribution du stress de surface dans le gyre de Beaufort.

Nos résultats montrent qu'une pente topographique plus large augmente le transport du gyre, cohérent avec les conclusions de Manucharyan & Isachsen (2019). Cette topographie azimutale introduit un β topographique, relaxant la condition d'instabilité barocline localement, augmentant le transport. Nous montrons également qu'un meilleur alignement de la pente maximale avec les contraintes de surface constitue un contrôle clé sur l'amplitude du transport. L'incorporation d'un modèle de glace simplifié redistribue le maximum de la contrainte de surface pour s'aligner mieux avec la topographie, menant a un important effet de la glace en présence d'une topographie azimutale, contrairement à quand la pente azimutale est absente. La circulation de renversement n'a pas d'effet sur la relation entre les contraintes de surface et le transport quand la topographie azimutale est absente. Quand la pente topographique est comprise dans la configuration, la stabilisation de l'écoulement là où la circulation de renversement est la plus forte permet la circulation de renversement d'avoir une plus grande influence sur le transport, surtout à faible vent. Ce résultat est en adéquation avec celui de Youngs et al. (2019), qui montre que, dans une configuration de l'ACC sur un plan-β, une circulation de renversement influence surtout le transport à faible vent. Cette similarité entre nos résultats et ceux obtenus dans l'ACC souligne le parallèle entre le plan-β de l'ACC et le β topographique dans une configuration du gyre. Finalement, nous montrons l'effet important de la friction de fond. Conformément aux conclusions de Nilsson et al. (2024), nous observons que le transport augmente lorsque la friction de fond augmente. Nous montrons également l'effet d'une forte friction de fond sur la relation entre la contrainte de surface et le transport. Lorsque la friction augmente, le puits principal de quantité de mouvement bascule du TFS au frottement de fond, ce qui entraîne une augmentation dans le transport et une perte de la saturation. De plus, à haute friction, le transport de différentes configurations topographiques converge, ce qui nous permet de conclure qu'une forte friction de fond rend le transport insensible à la topographie du fond. L'augmentation du transport, la perte de saturation, et la convergence du transport associéés à une forte friction de fond que nous constatons dans notre étude sont toutes des comportements observés dans l'ACC (Nadeau & Straub, 2012; Nadeau & Ferrari, 2015; Bai et al., 2021; Marshall et al., 2017).

Comme toute étude basée sur des configurations idéalisées, elle comporte certaines limites. Le cadre quasi-géostrophique à deux couches, la représentation idéalisée de la topographie et l'emploi d'un modèle de glace fortement simplifié imposent des hypothèses qui restreignent la généralisation des résultats. Ces choix méthodologiques ont toutefois permis de cibler les mécanismes dominants, d'isoler leurs interactions, et d'établir des comparaisons cohérentes avec des résultats tout aussi idéalisés issus d'une configuration de l'ACC.

Les travaux présentés ouvrent également la voie à plusieurs pistes de recherche. L'utilisation d'un modèle aux équations primitives permettrait de tester la robustesse des mécanismes identifiés dans notre modèle idéalisé et d'évaluer dans quelle mesure ils se maintiennent dans une configuration plus réaliste. L'intégration d'une topographie et d'un modèle de glace plus représentatifs du gyre de Beaufort permettrait de mieux relier les conclusions obtenues ici aux observations et à la variabilité réelle de la région. Ces perspectives offrent des pistes pour approfondir notre compréhension des circulations de hautes latitudes.

ANNEXE I

VELOCITY DEPENDENT WIND STRESS

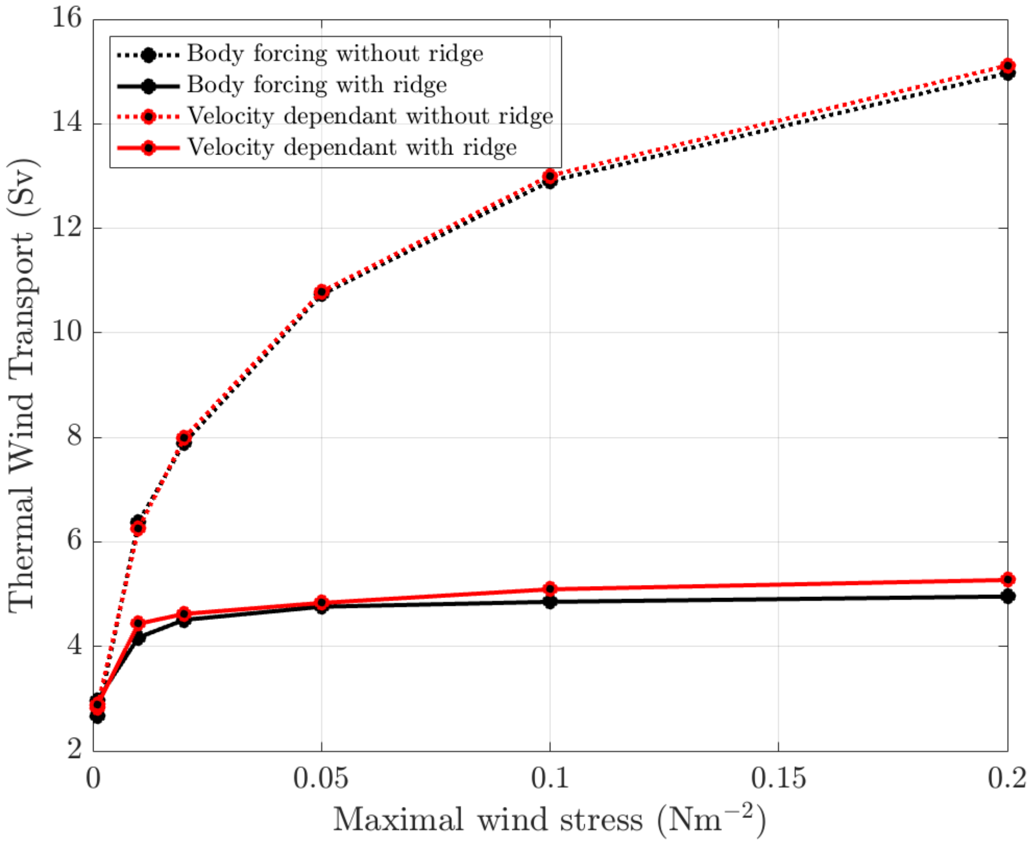

Figure 14 – Thermal wind transport of body forcing stress formulation (black curves) and velocity dependent stress formulation (red curves) with (solid curves) and without (dotted curves) radial topography. No azimuthal topography is applied.

The velocity dependent formulation of surface stress accounts for the relative velocities of the wind and ocean, defined as :

$$\tau^a = C_{da}\rho_a|\boldsymbol{u}_a - \boldsymbol{u_1}|(\boldsymbol{u}_a - \boldsymbol{u}_1).$$

This contrasts the body forcing formulation applied in the rest of the manuscript, defined as $\tau^a = C_{da}\rho_a|\boldsymbol{u}_a|\boldsymbol{u}_a$. We compare the thermal wind transports of these two formulations (fig. 14) and find minimal differences.

ANNEXE II

VARYING RIDGE LENGTH

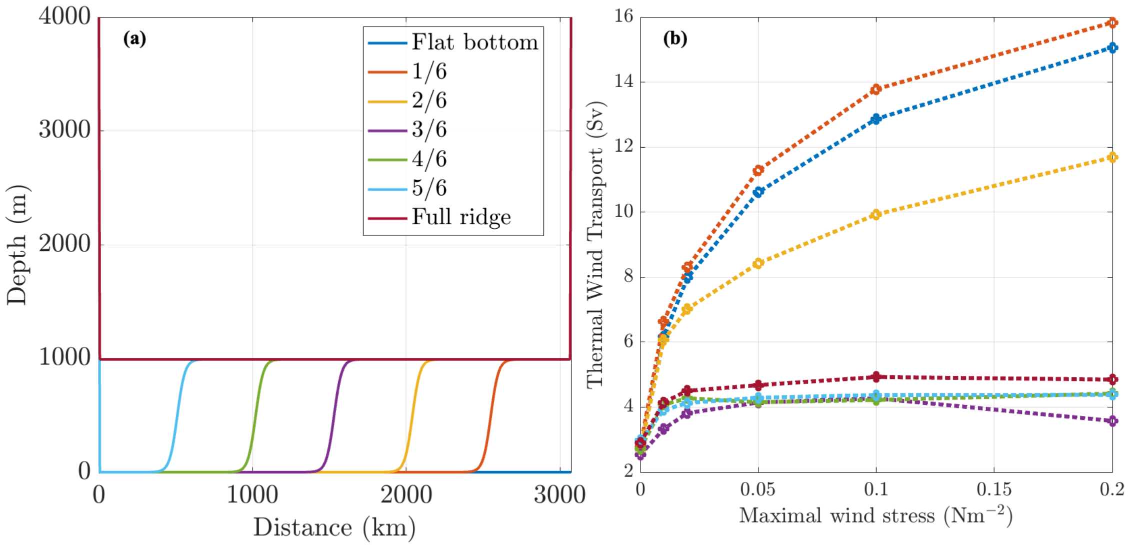

FIGURE 15 – (a) : Cross section at $y = L/2$ of topography with varying ridge lengths. (b) : Thermal wind transport (Sv) versus maximal wind stress for various ridge lengths.

Simulations without azimuthal topographic features, and with a ridge of varying extent (fig. 15a) were conducted at varying wind stress magnitudes (fig. 15b). When a ridge that spans at least half the domain width is applied, an eddy saturated state emerges. A ridge that spans 1/6 of the domain produces virtually identical thermal wind transports to the ridgeless case.

ANNEXE III

CONSTANT TOPOGRAPHIC β OF VARYING SLOPE

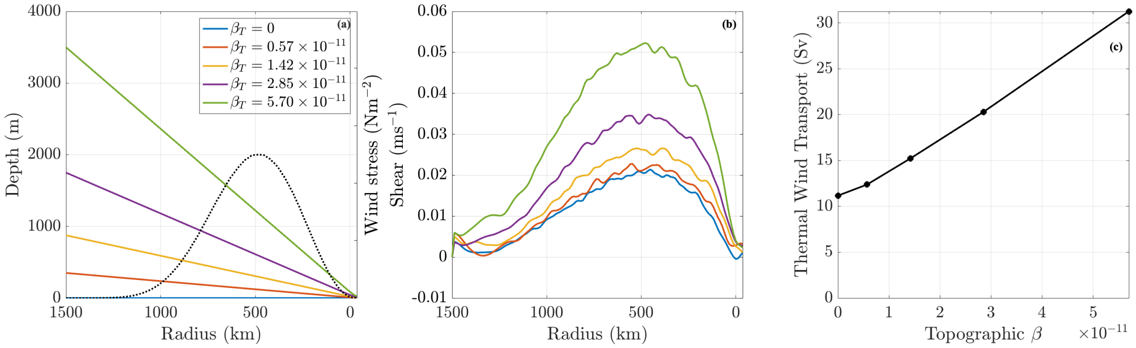

FIGURE 16 – (a) : Topography of various linear slope applied, with their correspondic topographic β (β_T) in the legend. Dotted curve represents normalized wind stress. The amplitude of the wind stress is $\tau_0 = 0.05$ Nm^{-2} for all simulations. (b) : Vertical shear of various constant topographic β simulations. (c) : Thermal wind transport for each topographic β.

Five simulations with a constant, linear sloping topography were conducted. This topography spans the total radius of the configuration, defining a cone-shape (fig. 16a). These supplementary simulations were performed at a coarser grid resolution ($dx = 12$km), with a Rossby radius $L_d = 10km$. As the slope steepens, the topographic β (β_T) increases, varying from $\beta_T = 0\text{m}^{-1}\text{s}^{-1}$ to $\beta_T = 5.7 \times 10^{-11}\text{m}^{-1}\text{s}^{-1}$. An increased topographic β leads to a stronger shear (fig. 16b), with thermal wind transport increasing linearly with β_T (fig. 16c).

RÉFÉRENCES

Arbic, B. K. & Scott, R. B. (2008). On quadratic bottom drag, geostrophic turbulence, and oceanic mesoscale eddies. *Journal of physical oceanography*, 38(1):84–103.

Bai, Y., Wang, Y., & Stewart, A. L. (2021). Does topographic form stress impede prograde ocean currents? *Journal of Physical Oceanography*, 51(8):2617–2638.

Beer, E., Eisenman, I., Wagner, T. J., & Fine, E. C. (2023). A possible hysteresis in the Arctic Ocean due to release of subsurface heat during sea ice retreat. *Journal of Physical Oceanography*, 53(5):1323–1335.

Carmack, E., McLaughlin, F., Yamamoto-Kawai, M., Itoh, M., Shimada, K., Krishfield, R., & Proshutinsky, A. (2008). Freshwater storage in the Northern Ocean and the special role of the Beaufort Gyre. In *Arctic–Subarctic ocean fluxes: defining the role of the northern seas in climate*, pages 145–169. Springer.

Carmack, E. & Wassmann, P. (2006). Food webs and physical–biological coupling on pan-arctic shelves: unifying concepts and comprehensive perspectives. *Progress in Oceanography*, 71(2-4):446–477.

Deng, P. & Wang, Y. (2024). Distinct impacts of topographic versus planetary pv gradients on baroclinic turbulence. *Journal of Physical Oceanography*, 54(10):2205–2231.

Doddridge, E. W., Meneghello, G., Marshall, J., Scott, J., & Lique, C. (2019). A three-way balance in the Beaufort Gyre: The ice-ocean governor, wind stress, and eddy diffusivity. *Journal of Geophysical Research: Oceans*, 124(5):3107–3124.

Gallet, B. & Ferrari, R. (2021). A quantitative scaling theory for meridional heat transport in planetary atmospheres and oceans. *AGU Advances*, 2(3):e2020AV000362.

Gill, A. (1968). A linear model of the Antarctic Circumpolar Current. *Journal of Fluid Mechanics*, 32(3):465–488.

Hallberg, R. & Gnanadesikan, A. (2001). An exploration of the role of transient eddies in determining the transport of a zonally reentrant current. *Journal of Physical Oceanography*, 31(11):3312–3330.

Isachsen, P. E., Vogt-Vincent, N. S., Johnson, H. L., & Nilsson, J. (2024). Instability and mesoscale eddy fluxes in an idealized 3-layer Beaufort Gyre. *Journal of Geophysical Research: Oceans*, 129(8):e2023JC020757.

Kwok, R. (2018). Arctic sea ice thickness, volume, and multiyear ice coverage: losses and coupled variability (1958–2018). *Environmental Research Letters*, 13(10):105005.

Lique, C., Johnson, H. L., & Davis, P. E. (2015). On the interplay between the circulation in the surface and the intermediate layers of the Arctic Ocean. *Journal of Physical Oceanography*, 45(5):1393–1409.

Manucharyan, G. & Isachsen, P. E. (2019). Critical role of continental slopes in halocline and eddy dynamics of the Ekman-driven Beaufort Gyre. *Journal of Geophysical Research: Oceans*, 124(4):2679–2696.

Manucharyan, G. E. & Spall, M. A. (2016). Wind-driven freshwater buildup and release in the Beaufort Gyre constrained by mesoscale eddies. *Geophysical Research Letters*, 43(1):273–282.

Manucharyan, G. E., Spall, M. A., & Thompson, A. F. (2016). A theory of the wind-driven Beaufort Gyre variability. *Journal of Physical Oceanography*, 46(11):3263–3278.

Manucharyan, G. E. & Stewart, A. L. (2022). Stirring of interior potential vorticity gradients as a formation mechanism for large subsurface-intensified eddies in the Beaufort Gyre. *Journal of Physical Oceanography*, 52(12):3349–3370.

Manucharyan, G. E., Thompson, A. F., & Spall, M. A. (2017). Eddy memory mode of multidecadal variability in residual-mean ocean circulations with application to the Beaufort Gyre. *Journal of Physical Oceanography*, 47(4):855–866.

Marshall, D. P., Ambaum, M. H., Maddison, J. R., Munday, D. R., & Novak, L. (2017). Eddy saturation and frictional control of the Antarctic Circumpolar Current. *Geophysical research letters*, 44(1):286–292.

Martin, T., Steele, M., & Zhang, J. (2014). Seasonality and long-term trend of Arctic Ocean surface stress in a model. *Journal of Geophysical Research: Oceans*, 119(3):1723–1738.

Mason, H. & Smith, K. S. (2025). Beaufort Gyre isopycnal structure produces a steady mesoscale eddy field modulated by sea ice drag. *Journal of Geophysical Research: Oceans*, 130(10):e2024JC022273.

Meneghello, G., Marshall, J., Campin, J.-M., Doddridge, E., & Timmermans, M.-L. (2018). The ice-ocean governor: Ice-ocean stress feedback limits Beaufort Gyre spin-up. *Geophysical Research Letters*, 45(20):11–293.

Meredith, M. P. & Hogg, A. M. (2006). Circumpolar response of Southern Ocean eddy activity to a change in the Southern Annular mode. *Geophysical Research Letters*, 33(16).

Munk, W. H. & Palmén, E. (1951). Note on the dynamics of the Antarctic Circumpolar Current 1. *Tellus*, 3(1):53–55.

Nadeau, L.-P. & Ferrari, R. (2015). The role of closed gyres in setting the zonal transport of the Antarctic Circumpolar Current. *Journal of Physical Oceanography*, 45(6):1491–1509.

Nadeau, L.-P. & Straub, D. N. (2012). Influence of wind stress, wind stress curl, and bottom friction on the transport of a model Antarctic Circumpolar Current. *Journal of physical oceanography*, 42(1):207–222.

Nilsson, J., Kallmyr, J.-A. H., & Isachsen, P. E. (2024). Topographic steering of the upper Arctic Ocean circulation by deep flows. *Tellus*, 76(1).

Polyakov, I. V., Rippeth, T. P., Fer, I., Alkire, M. B., Baumann, T. M., Carmack, E. C., Ingvaldsen, R., Ivanov, V. V., Janout, M., Lind, S., et al. (2020). Weakening of cold halocline layer exposes sea ice to oceanic heat in the eastern Arctic Ocean. *Journal of Climate*, 33(18):8107–8123.

Previdi, M., Smith, K. L., & Polvani, L. M. (2021). Arctic amplification of climate change: a review of underlying mechanisms. *Environmental Research Letters*, 16(9):093003.

Proshutinsky, A., Krishfield, R., Timmermans, M.-L., Toole, J., Carmack, E., McLaughlin, F., Williams, W. J., Zimmermann, S., Itoh, M., & Shimada, K. (2009). Beaufort Gyre freshwater reservoir: State and variability from observations. *Journal of Geophysical Research: Oceans*, 114(C1).

Rantanen, M., Karpechko, A. Y., Lipponen, A., Nordling, K., Hyvärinen, O., Ruosteenoja, K., Vihma, T., & Laaksonen, A. (2022). The Arctic has warmed nearly four times faster than the globe since 1979. *Communications earth & environment*, 3(1):168.

Regan, H. C., Lique, C., & Armitage, T. W. (2019). The Beaufort Gyre extent, shape, and location between 2003 and 2014 from satellite observations. *Journal of Geophysical Research: Oceans*, 124(2):844–862.

Serreze, M. C. & Barry, R. G. (2011). Processes and impacts of Arctic amplification: A research synthesis. *Global and planetary change*, 77(1-2):85–96.

Stern, A., Nadeau, L.-P., & Holland, D. (2015). Instability and mixing of zonal jets along an idealized continental shelf break. *Journal of Physical Oceanography*, 45(9):2315–2338.

Straub, D. N. (1993). On the transport and angular momentum balance of channel models of the Antarctic Circumpolar Current. *Journal of physical oceanography*, 23(4):776–782.

Thompson, A. F. (2010). Jet formation and evolution in baroclinic turbulence with simple topography. *Journal of Physical Oceanography*, 40(2):257–278.

Timmermans, M.-L. & Marshall, J. (2020). Understanding Arctic Ocean circulation: A review of ocean dynamics in a changing climate. *Journal of Geophysical Research: Oceans*, 125(4):e2018JC014378.

Timmermans, M.-L. & Toole, J. M. (2023). The Arctic Ocean's Beaufort Gyre. *Annual Review of Marine Science*, 15(1):223–248.

Vallis, G. K. (2017). *Atmospheric and oceanic fluid dynamics*. Cambridge University Press.

Wolff, J.-O., Maier-Reimer, E., & Olbers, D. J. (1991). Wind-driven flow over topography in a zonal β-plane channel: A quasi-geostrophic model of the Antarctic Circumpolar Current. *Journal of physical oceanography*, 21(2):236–264.

Yang, J., Proshutinsky, A., & Lin, X. (2016). Dynamics of an idealized Beaufort Gyre: 1. The effect of a small beta and lack of western boundaries. *Journal of Geophysical Research: Oceans*, 121(2):1249–1261.

Youngs, M. K., Flierl, G. R., & Ferrari, R. (2019). Role of residual overturning for the sensitivity of Southern Ocean isopycnal slopes to changes in wind forcing. *Journal of Physical Oceanography*, 49(11):2867–2881.

Yuan, X. & Martinson, D. G. (2000). Antarctic sea ice extent variability and its global connectivity. *Journal of Climate*, 13(10):1697–1717.

Zhang, J., Spitz, Y. H., Steele, M., Ashjian, C., Campbell, R., & Schweiger, A. (2020). Biophysical consequences of a relaxing Beaufort Gyre. *Geophysical Research Letters*, 47(2):e2019GL085990.

Zhao, M. & Timmermans, M.-L. (2015). Vertical scales and dynamics of eddies in the Arctic Ocean's Canada Basin. *Journal of Geophysical Research: Oceans*, 120(12):8195–8209.